IEEE Transactions on Quantum Engineering

Received 30 June 2022; revised 22 August 2022; accepted 2 September 2022; date of publication 7 September 2022; date of current version 5 October 2022.

Digital Object Identifier 10.1109/TQE.2022.3204928

Quantum Control of Optically Active Artificial Atoms With Surface Acoustic Waves

MICHAEL CHOQUER[1], MATTHIAS WEIß[2,3], EMELINE D. S. NYSTEN[2,3], MICHELLE LIENHART[2,3], PAWEŁ MACHNIKOWSKI[4], DANIEL WIGGER[4,5], HUBERT J. KRENNER[2,3], AND GALAN MOODY[1]

[1]Electrical and Computer Engineering Department, University of California, Santa Barbara, CA 93106 USA
[2]Physikalisches Institut, Westfälische Wilhelms-Universität Münster, 48149 Münster, Germany
[3]Lehrstuhl für Experimentalphysik 1 and Augsburg Centre for Innovative Technologies (ACIT), Universität Augsburg, 86150 Augsburg, Germany
[4]Department of Theoretical Physics, Wrocław University of Science and Technology, 50-370 Wrocław, Poland
[5]School of Physics, Trinity College Dublin, Dublin 2, Ireland

Corresponding authors: Daniel Wigger; Hubert J. Krenner; Galan Moody (e-mail: daniel.wigger@pwr.edu.pl; krenner@uni-muenster.de; moody@ucsb.edu).

This work was supported in part by the UC Santa Barbara NSF Quantum Foundry funded via the Q-AMASE-i Program under Award DMR-1906325, in part by the Deutsche Forschungsgemeinschaft (DFG, German Research Foundation) under Grant 465136867, and in part by the Bavaria-California Technology Center BaCaTeC (Förderprojekt Nr. 8 [2020-1]). The work of D. Wigger was supported by the Science Foundation Ireland (SFI) under Grant 18/RP/6236.

ABSTRACT Surface acoustic waves (SAWs) are a versatile tool for realizing coherent quantum interfaces between various solid-state qubits spanning microwave to optical frequencies. Through strain, electric, or magnetic fields associated with acoustic waves, qubit states can be controlled and measured with exquisite precision for applications in quantum information processing, memory, transduction, and sensing. In this review, we discuss progress toward quantum control using surface acoustic waves coupled to optically active artificial atoms, including semiconductor quantum dots (QDs), optically addressable solid-state spins, and quantum emitters in van der Waals materials. We outline the device, material, and theoretical considerations for realizing interactions with surface acoustic waves in the quantum regime, summarize the state of the art in coupling surface acoustic waves to artificial atoms, and provide insight into the current trends and trajectory of the field.

INDEX TERMS Quantum dots (QDs), quantum networking and communications, surface acoustic waves (SAWs).

I. INTRODUCTION

Today, surface acoustic waves (SAWs) are one of the few phononic technologies of industrial relevance. These surface-confined elastic waves find application in a wide range of disciplines, from radio-signal processing and wireless devices to acousto-fluidics, life sciences, and biological and chemical sensors [1]. In the last few years, elastic waves, and SAWs in particular, have become a versatile tool for controlling individual artificial atoms, including optically-active semiconductor quantum dots (QDs) [2], [3], [4], [5], electrostatically-defined QDs [6], [7], [8], defect centers in wide-bandgap materials [9], [10], [11], superconducting qubits [12], [13], [14], and van der Waals materials [15], [16]. The appeal of SAWs for quantum control is their flexibility: because they are hosted in piezoactive materials, they can couple to any quantum system through strain, electric, or magnetic fields [17]. This opens up the possibility to not only control individual quantum systems but also to serve as a universal quantum bus to connect dissimilar, remote systems whose interactions are mediated by the propagating acoustic waves.

The coupling between SAWs and artificial atoms can be deliberately enhanced by confining both systems to an acoustic resonator. Placing the atomlike system at one of the antinodes of the SAW resonator's strain, electric, or magnetic fields enables large interactions between the two subsystems, establishing an acoustic analog to cavity and circuit quantum electrodynamics known as quantum acoustics. The anatomy of a SAW resonator is illustrated in Fig. 1. It typically comprises either a piezoactive host material, such as lithium

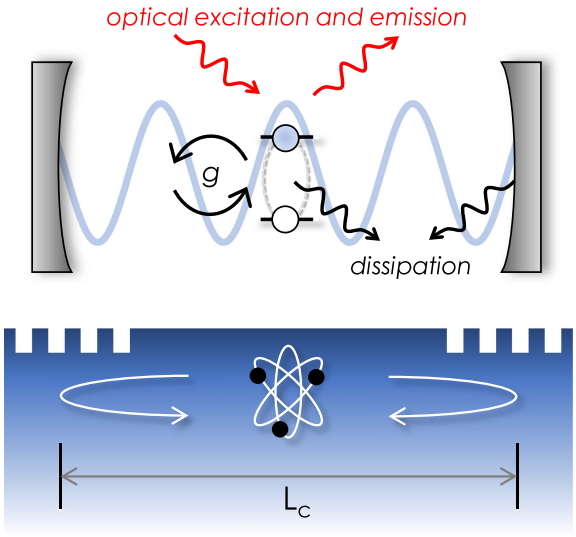

FIGURE 1. Anatomy of a SAW resonator for quantum control. An artificial atom embedded within or near the surface of piezoelectric material couples to surface-confined acoustic modes through strain, electric, or magnetic fields. DBRs created from grooves in the surface form the acoustic cavity with length L_c. The resonator and atom experience different dissipation mechanisms, which contribute to their respective linewidths κ_M and κ_A.

niobate ($LiNbO_3$) or aluminum gallium arsenide (AlGaAs), or a thin film of piezoactive aluminum nitride (AlN) or deposited zinc oxide (ZnO) on a nonpiezoactive or a weakly piezoactive substrate, for instance silicon, zinc telluride, and diamond. Distributed Bragg reflectors (DBRs) made from patterned metal or grooves etched into the substrate form the acoustic resonator with an effective cavity length L_c. The fundamental mode of the resonator is given by $f_c = v_s/2\Lambda$, where Λ is the period of the mirror corrugations and v_s is the phase velocity of the SAW in the material, typically on the order of 10^3 m/s.

In piezoelectric materials, SAWs can be generated by using lithographically patterned interdigital transducers (IDTs) within or outside of the resonator with frequencies spanning a few megahertz (MHz) to more than 30 GHz [18]. SAWs offer several advantages for controlling quantum systems in comparison to other optomechanical approaches, including GHz operation frequencies [19], [20] that allow for passive ground-state cooling from the cryogenic system, coupling to artificial atoms through a variety of mechanisms [1], [17], [21], modal confinement to within an acoustic wavelength from the surface [22], [23], and large feature sizes and a planar geometry that is straightforward to fabricate [10], [24].

Coupled artificial atom–SAW platforms have reached various levels of device and control complexity, as illustrated in Table 1. Systems in Stage 1 demonstrate SAW–artificial atom coupling with propagating SAWs that are not in the quantum regime; this has been achieved for numerous artificial atom systems, including QDs [2], spins in defect centers [9], layered materials [16], and superconducting circuits [12]. Operation in Stage 1 is analogous to interactions between artificial atoms and open transmission lines in circuit quantum electrodynamics, whereby a large number of coherent propagating phonons can be described by classical wave theory and the artificial atom is treated quantum mechanically. Stage 2 is a transition toward the quantum regime as described by quantum acoustics, where SAW resonator modes couple to an artificial atom, yet the SAW–artificial atom system is not in the quantum regime and so can be described by semiclassical theory. Most technologies have reached this stage of complexity [10], [25], [26], with the exception of layered materials due to their relatively recent discovery. Stage 3 is reached when both the SAWs and artificial atoms are operating in the quantum regime. Stages 2 and 3 can qualitatively be distinguished by the cooperativity, defined as $\mathcal{C} = g^2/(\kappa_M\kappa_A)$, which compares the product of the decoherence rates of the artificial atom κ_A and SAW cavity κ_M with their coupling strength g. In general, κ_M includes both damping and thermal decoherence channels, and κ_A includes both radiative and nonradiative decay as well as pure dephasing mechanisms.

When the cooperativity exceeds unity plus the thermal phonon population in the cavity, $\mathcal{C} > \bar{n}_{th} + 1$, the SAW–artificial atom system enters the quantum regime (Stage 3), enabling a variety of quantum phenomena to be observed [17]. Currently, Stage 3 has only been achieved with superconducting circuits [13], [24], [27], [28], although these demonstrations required a large number of SAW cavity phonons $\bar{n}_{cav} \gg 1$ to enhance the interaction via $g = \sqrt{\bar{n}_{cav}}g_0$, where $\bar{n}_{cav}$ is the average SAW nonthermal cavity population and g_0 is the SAW–artificial atom vacuum coupling strength. An outstanding challenge in quantum acoustics is reaching the vacuum strong cooperativity regime $g_0 \gg \sqrt{\kappa_M\kappa_A}$, where the coupling between the SAW resonator and artificial atom overcomes the intrinsic dissipation of both systems [29]. An even stronger condition is realizing the vacuum strong coupling regime, where the two subsystems can coherently exchange energy quanta [30]. Such a regime would enable deterministic entangling gates between single SAW phonons and artificial atoms and arbitrary quantum state transfer [17].

One of the essential elements of quantum control with SAW resonators is coherent interaction with artificial atoms, determined by the quality factor and mode volume of the resonator. The cooperativity $\mathcal{C}$ is directly proportional to the SAW quality factor, $Q \sim 1/\kappa_M$, which determines the loss rate of phonons from a SAW resonator. $\mathcal{C}$ is also heavily impacted by the coupling strength between a single SAW resonator phonon and an artificial atom, which can be defined as $g_0 = \chi\epsilon_{ZPM}$ where ϵ_{ZPM} is the dimensionless zero-point volumetric strain amplitude of the SAW resonator ground state and χ is a mechanical susceptibility parameter related to the strain, electric, or magnetic field coupling between the SAW and artificial atom. The SAW zero-point strain amplitude is defined as $\epsilon_{ZPM} = (2\pi/\lambda)\sqrt{\hbar/(2\rho v_s A)}$, where ρ is the density of the SAW substrate, v_s is the SAW phase velocity, A is the SAW effective area in the plane of the substrate, and λ is the acoustic wavelength. For typical SAW materials in crystalline substrates, $\epsilon_{ZPM} \approx 10^{-8}$ for a SAW confined to $A \approx 1$

IEEE Transactions on Quantum Engineering

TABLE 1 Comparison of Various SAW–Artificial Atom Technologies and Their Stages of Development, From Classical Control With Propagating SAWs (Stage 1) and Resonator-Confined SAWs (Stage 2) to Quantum Acoustic Control (Stage 3)

 Artificial Atom–SAW system	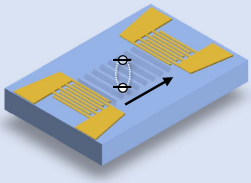 **Stage 1** Classical control propagating SAWs	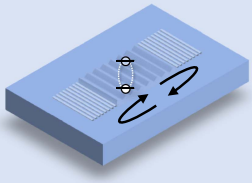 **Stage 2** Classical control SAW resonator	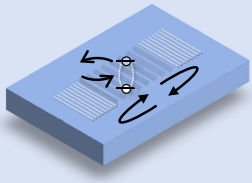 **Stage 3** Quantum control SAW resonator
Quantum dot excitons	✓ Refs. [2]–[5]	✓ Refs. [52], [63]	✗
Defect center spins	✓ Ref. [9]	✓ Ref. [10], [11]	✗
Layered materials	✓ Ref. [16]	✗	✗
Superconducting circuits	✓ Ref. [12]	✓ Ref. [20]	✓ Ref. [13]

μm ^{2} [17]. Characterizing SAW susceptibility parameters for various artificial atoms is still an active area of research, though values for some systems are available. For InAs self-assembled QDs [3], [31], SiV^- centers in diamond [32] and defects in hexagonal boron nitride (hBN) [16], χ is on the order of 10 THz/%. The respective decoherence rates of these artificial atoms are $\kappa_A < 1$ GHz [19], [33], $\approx$1 GHz [34], and $\approx$50 MHz, respectively [35]. The above data for SAW zero-point strain amplitude, quality factor, and artificial atom mechanical susceptibility and linewidth indicate the cooperativity may approach or even exceed unity for SAW resonators cooled to their ground state ($\bar{n}_{th} = 0$), opening a realm of possibilities in quantum information processing [17].

In the remainder of this article, we provide an overview of SAW–artificial atom coupling in the various aforementioned platforms, with a focus on optically active systems. In Section II, we present the background content of SAW resonators and theoretical treatment of artificial atom–SAW coupling and spin–SAW coupling. In Section III, we discuss experimental implementations of SAW coupling to excitons in QDs, orbitals and spins in defect centers, and optically active defects in layered materials. We conclude with an outlook on future directions for quantum control using SAWs.

II. THEORETICAL BACKGROUND

A. SAW RESONATORS AND IDTS

The quality factor Q of SAW resonators is limited by several decay channels, including intrinsic material loss, diffraction causing SAW energy to escape from the resonator cross-section, SAW conversion to bulk modes, SAW leakage from the resonator mirrors, and SAW transduction to microwave photons via the IDTs. Q for SAWs can be divided into two components as $1/Q = 1/Q_i + 1/Q_e$, where the internal and external quality factors, Q_i and Q_e, respectively, represent the limits from SAW decay and from dissipative coupling to IDTs. Also known as the unloaded quality factor, Q_i includes intrinsic material, diffraction, bulk scattering, and SAW mirror leakage decay channels, and it represents the ultimate achievable quality factor for a particular SAW resonator design in the limit of vanishing acoustic loss from IDTs [36]. Measurements of Q for state-of-the-art gigahertz SAW resonators at millikelvin temperatures show $Q_i > 10^5$ for low-loss quartz [20] GaAs [28] and ZnO [37] substrates, and $Q \approx 10^4 - 10^5$ for gigahertz-frequency SAW resonators at cryogenic temperatures in $LiNbO_3$[38], [39].

Unlike electromagnetic resonators in the microwave and optical domains, high-quality SAW resonators cannot be constructed from localized reflectors [36], which strongly scatter SAWs to bulk acoustic waves. Instead, high-Q SAW resonators are created using DBRs. Analogous to optical Bragg grating mirrors, for SAWs, small periodic perturbations to the surface-wave velocity result in an appreciable reflection coefficient when distributed over many acoustic wavelengths. These reflectors suppress surface-to-bulk mode scattering because SAWs have a lower acoustic velocity than bulk waves, shifting the coherent coupling to bulk modes above the SAW grating's upper stopband edge [see Fig. 2(d), blue]. For comparison, Fig. 2(c) shows the bulk (shaded) and SAW dispersion for an unpatterned surface, where the SAW bands (green and blue lines) intersect and do not show a bandgap at the edge of the Brillouin zone. Fig. 2(d) shows a bandgap that appears for a periodic SAW mirror unit cell. SAW gratings are commonly realized either through metallic strips deposited on a piezoelectric substrate surface or by etching grooves in the substrate [see Fig. 2(a)] to couple propagating SAWs from the left and right [38]; grooves typically produce resonators with higher quality factors for materials with lower piezoelectric coupling, such as GaAs [40], [41]. A unit cell of such a SAW DBR is schematically represented in Fig. 2(a) with the characteristic design parameters being the etched groove depth h and period Λ.

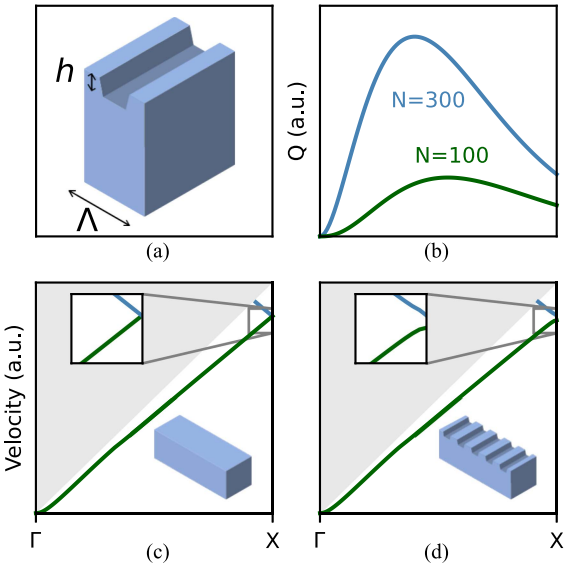

FIGURE 2. **(a) Schematic of a SAW mirror unit cell of period Λ with etched grooves of depth *h*. (b) Qualitative relationship between groove-based SAW resonator quality factor and the etched groove depth for two mirrors with groove numbers $N = 100$ (green) and $N = 300$ (blue). (c) Bandstructure of an unpatterned surface showing degenerate Rayleigh SAW modes (blue and green lines) and bulk mode continuum (shaded). (d) Bandstructure of SAW phononic crystal showing the upper and lower Rayleigh SAW band edge modes, with stopbands and a bandgap directly proportional to the SAW mirror unit cell reflection strength.**

Fig. 2(b) shows the relationship between the quality factor of a SAW resonator and the etched groove depth of the mirrors for two different total groove numbers $N = 300$ (blue) and $N = 100$ (green). For smaller etch depths, the reflection per groove is lower, requiring longer gratings with more grooves to achieve high SAW reflection. Consequently, the quality factor of a SAW resonator with finite mirror length will be limited by leakage losses for relatively small groove depths, typically on the order of 1% of the acoustic wavelength [17], [40]. Although increasing the etch depth will increase the mirror reflection, deeper grooves also increase SAW scattering to bulk modes, eventually limiting Q_i for larger groove depths. SAW-to-bulk mode conversion occurs predominantly near the boundaries of the SAW resonator mirrors [42], where SAWs propagating in the unpatterned free surface comprising the SAW cavity region experience a mode conversion process when entering the grating [lower-right insets of Fig. 2(c) and (d)]. One approach to mitigate bulk mode conversion in SAW resonators is to add a transition region between the mirrors and the central cavity region, where the parameters of the SAW groove unit cell [see Fig. 2(a)] are varied adiabatically. This transition has been achieved by tapering the groove depth toward the ends of the gratings [42]. Alternatively, a localized SAW defect state can be engineered in the middle of the mirror bandgap by patterning the entire SAW resonator in a grating structure with an adiabatic transition from the groove period in the mirrors to a greater period in the central cavity region [38]. The latter approach is equivalent to creating a Wannier envelope function for the SAW mode in both real and reciprocal space [43], which confines the mode to near diffraction-limited volume, increasing the SAW amplitude interacting with artificial atoms while preserving a high Q_i.

Realizing the quantum regime with artificial atoms is motivating further improvements in SAW resonator design. Focusing IDTs (FIDTs) and cavities are used to laterally confine SAWs, limiting diffraction losses [10], [49], [51], [52] while also concentrating SAW modes to diffraction-limited length scales [53]. One challenge for focusing resonators and cavities is the SAW velocity angular dispersion in acoustically anisotropic crystalline materials. Realizing high-Q resonators with anisotropic piezoelectrics will require precise knowledge of the elastic and piezoelectric material constants and tight process control over the FIDT angular alignment [40], [54]. Alternatives to FIDTs and focusing cavities are being actively pursued, including focusing through acoustic lens structures [55] and SAW 2-D phononic crystal structures with complete, omnidirectional SAW bandgaps [56], [57].

Critical to driving SAW–artificial atom systems and measuring their nonclassical correlations is a low-loss interface to microwave circuitry. Ultralow-loss IDTs are being developed to enable high-fidelity, single-shot, and single-phonon readout of SAWs, similar to measurements routinely performed with microwave qubits at millikelvin temperatures [58]. IDTs are composed of periodic metallic electrodes, which upon applied microwave power, induce a time-varying strain on the underlying piezoelectric substrate or thin film through the inverse piezoelectric effect. By time-reversal symmetry, the reverse process allows IDTs to detect SAWs. IDTs can be designed to excite SAWs over a certain frequency bandwidth; the SAW amplitude generated over this bandwidth depends on material parameters, including the piezoelectricity K^2 and the effective capacitance C_S for a single IDT pair, as well as several device parameters, such as the number of IDT periods, the IDT electrode polarity sequence, and the IDT aperture width [40]. As a linear electrical device, IDTs can be matched efficiently to microwave transmission lines typically operating with an impedance of 50 Ω. IDT impedance matching is important for maximizing the conversion efficiency of microwave photons to SAW phonons and vice versa, which can be quantified through an efficiency value known as the reflection coefficient of power, defined as the ratio of the power dissipated by an IDT to the applied signal power from a microwave source [59]. The IDT reflection coefficient of power can also be expressed as a loss value known as the insertion loss [40]. For quantum applications, improving the IDT power efficiency is highly desirable, motivating research in unidirectional SAW transducers [60], [61], [62] that break mirror symmetry in the IDT unit cell to launch SAWs predominantly in one direction. Alternatively, IDTs placed in the central cavity region of SAW resonators [10], [21], [27], [28], [63] eliminate insertion loss from reflection from outside of the cavity. Loss in IDTs can

IEEE Transactions on Quantum Engineering

TABLE 2 Properties of Common SAW Materials, Where *Cut/Dir.* Is the Crystal Cut and SAW Propagation Direction, K^2 Is the Piezoelectric Coupling Coefficient, C_S Is the Effective Capacitance of an IDT Electrode Pair for a Single-Electrode Polarity Sequence [40], γ Is the Diffraction Coefficient, v_0 Is the SAW Bare Substrate Velocity, v_{eff} Is the SAW Velocity Including Electrical and Mechanical Loading From IDTs, α_{visc} Is the Upper Bound on the Viscous Damping of the Material, and Exp. $Q_i \times f$ Is the Highest Demonstrated Intrinsic Quality Factor-Resonant Frequency Product in SAW Resonators Designed for Quantum Applications ($f \approx$ GHz)

	Material / Temp.	$LiNbO_3$	GaAs	Quartz	ZnO	AlN
Cut/Dir.		128° Y-X	(001)-⟨110⟩	ST-X	(002)	(0001)-[1100]
K^2 (%)	300 K	5.4 [40]	0.064 [44]	0.12 [40]	1.07 [45]	0.25 [46]
C_S (pF/cm)	300 K	5.6 [40]	1.2 [47]	0.56 [40]	0.98 [21]	0.85 [48]
Diffraction γ	300 K	−0.35 [40]	−0.46 [49]	0.38 [40]	–	–
v_0 (m/s)	300 K	3979 [40]	2864 [47]	3159 [40]	–	5790 [46]
v_{eff} (m/s)	10 mK	3911 [50]	2880 [13]	3140.6 [26]	2680 [37]	–
α_{visc} (dB/cm)	10 mK	0.3 [39]	0.07 [28]†	0.065 [20]	–	–
Exp. $Q_i \times f$ (Hz)	10 mK	1.13×10^{14} [39]††	1.0×10^{15} [28]	3.43×10^{14} [20]	2.50×10^{14} [37]	–

†: Viscous propagation loss, α_{visc} extracted from the intrinsic quality factor, mirror separation, wave velocity, and free spectral range [20], [40].
††: Intrinsic quality factor extracted as $Q_i \approx Q$.

be reduced further by electrodes made from low-temperature superconductors, which show significant improvements below the superconducting critical temperature [37], [61].

Using classical wave theory, SAW resonators and IDTs are analyzed and designed through either the coupling-of-modes formalism or the reflective array method [40]. Finite-element methods [64] are commonly employed to extract coupling-of-modes parameters of periodic unit cells [65] and to match SAW mode profiles to the reflection spectra of IDTs [66] and SAW resonators [38]. The unit cell response can then be cascaded with other grating and IDT unit cells to determine the SAW device's scattering properties, characterized by the *P*-matrix [67], [68]. SAW resonators and IDTs are also modeled through equivalent circuit representations [21], [69], including the Butterworth Van Dyke circuit [70], which can be characterized empirically through measurements of the S_{11} scattering parameter [40], [71] and has been extended to the quantum regime [72].

B. MATERIALS FOR SAW DEVICES

Table 2 shows several low-loss piezoelectric SAW materials that are commonly used in quantum applications, each with tradeoffs in SAW-specific properties and integration with artificial atoms. As discussed in Section II-A, the piezoelectric or electromechanical coupling coefficient K^2 and the effective capacitance C_S for an IDT electrode pair determine the IDT frequency bandwidth and the capacitance of the IDT, the latter important for impedance matching [40]. Other important parameters for SAW materials are the diffraction γ, wave velocity v_0, and propagation loss α. SAW propagation loss has contributions from both wave diffraction and viscous material losses; upper bounds on the loss from viscous damping at millikelvin temperatures can be estimated from known quality factors of SAW resonators [21] or by the insertion loss measurements of SAW delay lines [60].

Two of the most common materials for classical SAW technologies are $LiNbO_3$ and quartz [40]. $LiNbO_3$ has exceptionally high piezoelectric coupling compared to other SAW materials, which increases the electromechanical coupling to IDTs; however, materials with greater piezoelectricity will also possess a greater susceptibility to stray electric fields, increasing environmental dissipation and decoherence. Low-piezoelectricity substrates such as quartz [20] and GaAs [28] have demonstrated high $Q_i \times f$ factors, the latter exceeding 10^{15} Hz. In a quartz resonator, Manenti et al. [20] observed that in the quantum regime, the internal quality factor decreases for pump drives approaching the single-phonon level to approximately $Q_{i0} \approx 0.6 \times Q_i$, which the authors attribute to coupling to a bath of two-level systems (TLSs). Other material platforms may have different TLS contributions to losses, including impurity ion ensembles [73].

In addition to single-crystal SAW substrates, numerous SAW material heterostructures consist of a thin film of piezoelectric material deposited on a host substrate, facilitating efficient SAW generation in materials without a strong intrinsic piezoelectric response. Such heterostructures are present in many of the works featured in this review [9], [10], [11], [23], [74], [75], [76], [77] and allow tailoring of the SAW properties, including velocity, diffraction, and piezoelectricity [66], [78], [79], [80]. SAW material heterostructures can also support multimode acoustic waveguiding for "slow-on-fast" heterostructures consisting of an acoustically soft thin film deposited onto a stiff substrate [44], [46].

Some piezoelectric overlayer materials also have favorable properties for SAW substrates operating in the quantum regime. Bulk ZnO is readily available in a wafer scale and becomes a low-loss SAW material at cryogenic temperatures, with SAW resonators exhibiting $Q_i \approx 1.5 \times 10^5$ [37]. A recent discovery of room-temperature quantum emission in crystalline AlN [81] could be a promising step toward an artificial atom–SAW material platform with a piezoelectric coupling comparable to that in ST-cut quartz and nearly an order of magnitude larger than in GaAs [46].

With the rapid exploration of thin-film $LiNbO_3$ [82], new opportunities are available for hybrid and heterogeneously integrated SAW material heterostructures. Hybrid integration, including transfer printing and microprobe-based pick-and-place and transfer methods [83], allows prefabricated structures with embedded artificial atoms to be aligned precisely to SAW devices [84], [85], [86]. Heterogeneous integration involves epitaxial liftoff or wafer bonding of

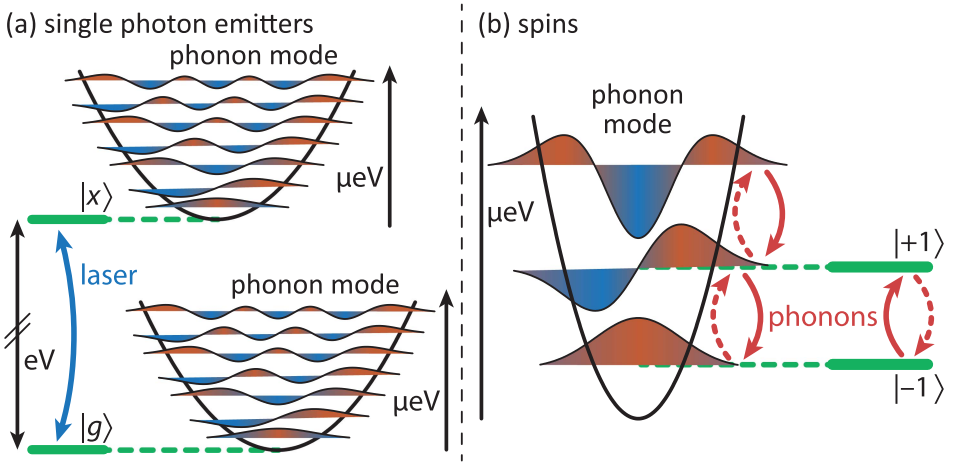

FIGURE 3. Schematic picture of the interaction between quantum systems and phonons. (a) For single-photon emitters, the typical Franck–Condon physics is found where the phonon energies are much smaller than optical transitions. (b) For spin systems, the transitions can be in resonance with phonon energies.

materials hosting artificial atoms to a desired piezoelectric SAW substrate [25]. Such hybrid and heterogenously-integrated heterostructures tailor the material properties of the photonic, acoustic, and microwave degrees of freedom, even allowing for simultaneous modal confinement [87]. Future SAW material heterostructures will integrate strong piezoelectric materials for efficient SAW electromechanical coupling with bright quantum emitters and ultralow-loss acoustic and microwave substrates, including quartz [20] and sapphire [88].

C. ARTIFICIAL ATOM–SAW COUPLING

As discussed in more detail in the following sections, artificial atoms with strong optical responses in the infrared to the visible range are promising building blocks for quantum technologies that rely on the controlled emission of photons [89]. Theoretically, such systems are successfully described by few-level systems. As we are here dealing with artificial atoms hosted by solids, these systems naturally interact with the lattice vibrations, i.e., the phonons, of the host material, and we are particularly interested in the interplay with SAW fields. A first estimate for the type of coupling can be gained by comparing the energy scales of the two systems: The artificial atoms have optically active transitions with energies in the range of electron-volts (eV) and interband transitions in the 10-meV range while typical SAW frequencies span a few gigahertz, i.e., in the μeV, range. Already this enormous mismatch shows that phonons cannot promote direct transitions between ground and excited states. The well-established independent Boson (IB) model takes this fact into account and only couples phonons to the excited state via the Hamiltonian [90]

$$H_{\mathrm{IB}} = E_{\mathrm{g}}\,|g\rangle\langle g| + E_{\mathrm{x}}\,|x\rangle\langle x| + g_{\mathrm{IB}}(b+b^{\dagger})\,|x\rangle\langle x| + \hbar\omega_{\mathrm{ph}} b^{\dagger}b \tag{1}$$

where $|g\rangle$ and $|x\rangle$ are ground and excited state, respectively, with the transition energy $E_{\mathrm{x}} - E_{\mathrm{g}}$. $b^{(\dagger)}$ are phonon operators and g_{IB} is the coupling strength (referred to as g_0 in the introduction). This model has the advantage that it can be diagonalized analytically by applying the so-called polaron transformation with $S = \dfrac{g_{\mathrm{IB}}}{\omega_{\mathrm{ph}}}(b^{\dagger} - b)|x\rangle\langle x|$ leading to

$$H_{\mathrm{IB}}^{P} = e^{S} H_{\mathrm{IB}} e^{-S} = \left(E_x - \frac{g_{\mathrm{IB}}^2}{\hbar\omega_{\mathrm{ph}}}\right)|x\rangle\langle x| + \hbar\omega_{\mathrm{ph}} b^{\dagger}b \tag{2}$$

where we have set $E_g = 0$. The transformed excited state $e^{S}|x\rangle$ is called the polaron. This Hamiltonian describes the situation schematically visualized in Fig. 3(a) usually associated with the Franck–Condon principle [91]. Each of the states of the TLS defines a different equilibrium position upon which the phonon states are built. The displacement of the two phonon parabolas is determined by the relative phonon coupling strength $g_{\mathrm{IB}}/(\hbar\omega_{\mathrm{ph}})$. Here, optical excitations usually have to be treated in a perturbative way [92].

Another approach to treat the IB Hamiltonian is by introducing generating functions of the form [93], [94]

$$Y(\alpha) = \left\langle |g\rangle\langle x|\, e^{-\alpha^* b^{\dagger}} e^{\alpha b} \right\rangle \tag{3a}$$

$$C(\alpha) = \left\langle |x\rangle\langle x|\, e^{-\alpha^* b^{\dagger}} e^{\alpha b} \right\rangle \tag{3b}$$

$$F(\alpha) = \left\langle e^{-\alpha^* b^{\dagger}} e^{\alpha b} \right\rangle. \tag{3c}$$

This approach allows one to consider the optical driving without any approximations. The system can also be treated exactly in the framework of path integrals [95].

In the IB model, one can in principle consider an arbitrary initial phonon state. Several theoretical works have studied how specific optical excitations change the phonon state [96], [97]. It was, for example, shown that phonon squeezing can be reached when the phonons are initially in the vacuum

state [98]. However, when interfacing an artificial atom with a traveling SAW field, the phonons are initially in a classical state. The limit of a classical state of a Boson field can be described by a coherent state fulfilling $b|\beta\rangle = \beta|\beta\rangle$ [99]. Then, we can replace the IB coupling Hamiltonian by [100]

$$g_{\mathrm{IB}}(b+b^\dagger)\,|x\rangle\langle x| \rightarrow 2g_{\mathrm{IB}}\mathrm{Re}(\beta)\,|x\rangle\langle x| = \Delta(t)\,|x\rangle\langle x| = H_{\mathrm{IB,SC}} \quad (4)$$

which we will refer to as semiclassical (SC) limit. Given that the coherent state has a harmonic time dependence with the frequency of the considered phonon mode ω_{ph}, this describes an energy modulation of the transition energy $E_1 + \Delta(t)$ in the full system.

Typically, for SAWs, the dominant coupling mechanism is the deformation potential, which is proportional to the trace of the local strain tensor $\Delta \sim \mathrm{Tr}(\boldsymbol{\varepsilon})$. The transition regime between the full quantum treatment of the IB model and its semiclassical limit has recently been explored systematically, employing the generating functions introduced before [101]. It was shown how photon scattering spectra and the considered phonon state change when approaching the ultimate quantum limit of an initial vacuum state from a coherent state with a large initial coherent amplitude $\beta \gg 1$.

D. SPIN–SAW COUPLING

Here, we want to consider atomic defect structures as prototypically represented by the nitrogen-vacancy (NV) center in diamond. Already when looking at the typical energy splittings among the spin states, we are dealing with a few μeV, which is automatically in the same range as the considered phonon energies. This shows that phonon-assisted transitions between the different spin states should in principle be possible. To find the coupling between the spin structure of such a defect and the lattice vibrations, one has to consider the specific symmetry of the system. We will consider the NV^- center in the following, as it is so far the most intensively investigated system.

The NV center possesses a spin-1 ground state manifold, i.e., we are dealing with the basis states $|+1\rangle$, $|0\rangle$, and $|-1\rangle$. The transition energies between these states can, for example, be tuned by applying a magnetic field, which is routinely used in optically detected magnetic resonance (ODMR). The NV center has an additional excited state with transition energy in the visible range. This state falls under the situation described in Section II-C, as discussed in more detail later.

By applying group theoretical arguments, it was shown that the coupling between the NV ground state spin system with C_{3v} symmetry and a given strain field can be written in the form [102]

$$\begin{aligned} H^{\mathrm{NV}}_{\text{spin-strain}} = {} & \gamma_0(\boldsymbol{\varepsilon})\,(|+1\rangle\langle+1| + |-1\rangle\langle-1|) \\ & + \gamma_{01}(\boldsymbol{\varepsilon})\,(|0\rangle\langle+1| - |0\rangle\langle-1|) + \mathrm{h.c.} \\ & + \gamma_{11}(\boldsymbol{\varepsilon})\,|-1\rangle\langle+1| + \mathrm{h.c.} \end{aligned} \quad (5)$$

where γ_0 is a real and $\gamma_{0,1}$, $\gamma_{\pm1}$ are complex functions of the strain tensor $\boldsymbol{\varepsilon}$. While the first term with γ_0 describes energy renormalizations of the states $|\pm1\rangle$, the other two terms promote mixing between the different spin states. Note that, in case of SAWs, the components of the strain tensor carry harmonic time dependencies. In many cases, only the last term is considered, especially in cases where an additional microwave field resonantly drives the transitions between $|0\rangle$ and $|\pm1\rangle$ [10], [76].

In direct analogy with the procedures carried out when deriving the Jaynes–Cummings model in quantum optics [103], here we can quantize the strain field and introduce the phonon operator $b^{(\dagger)}$. Then, the Hamiltonian describing state mixing and phonon-assisted transitions takes the general form

$$\begin{aligned} H^{\mathrm{NV}}_{\text{spin–phonon}} = {} & g_0(\boldsymbol{\varepsilon})\left(b^\dagger + b\right)(|+1\rangle\langle+1| + |-1\rangle\langle-1|) \\ & + g_{01}(\boldsymbol{\varepsilon})b^\dagger\,(|0\rangle\langle+1| - |0\rangle\langle-1|) + \mathrm{h.c.} \\ & + g_{11}(\boldsymbol{\varepsilon})b^\dagger\,|+1\rangle\langle+1| - \mathrm{h.c.} \end{aligned} \quad (6)$$

where we assume the energetic ordering $E_{+1} > E_{-1} > E_0$ and we applied the usual rotating wave approximation. The situation described by the last term is schematically visualized in Fig. 3(b), where the decay within the spin states is associated with the creation of a phonon and vice versa. A model of this form has, for example, been applied to simulate the phonon-mediated coupling between distant spin systems [17], [104].

III. EXPERIMENTAL IMPLEMENTATION

A. DYNAMIC CONTROL OF QD EXCITONS

QDs are an important building block for quantum technologies as they are an efficient source for both single and indistinguishable photons, as well as entangled photon pairs [105], [106]. Inside a QD, the motion of charge carriers is confined in all three spatial dimensions, resulting in their discrete energy spectrum; the solid-state nature of QDs makes them strongly susceptible to strain. Strong sensitivity to strain has traditionally been considered a drawback, since this can lead to, for example, appreciable phonon-induced dephasing of the QD [107], [108]. In recent years, however, several groups have leveraged this coupling to control QD excitonic emission via the strain field associated with a SAW, as long as the QD is located close to the surface of the substrate, typically within one acoustic wavelength. The interaction between a QD and a SAW is based on the deformation potential coupling that leads to a type-I band edge modulation and, therefore, to a dynamic modulation of the transition energy of a QD exciton as introduced in Section II-C.

The most studied types of QDs are InAs QDs embedded in a GaAs matrix and GaAs QDs embedded in an (Al)GaAs matrix. These material systems have the advantage of being piezoelectric, albeit weakly compared to other materials such as $LiNbO_3$. Nonetheless, they enable a direct excitation of SAWs using IDTs on the host substrate. The dynamic modulation of QDs by SAWs was also recently expanded to CdTe

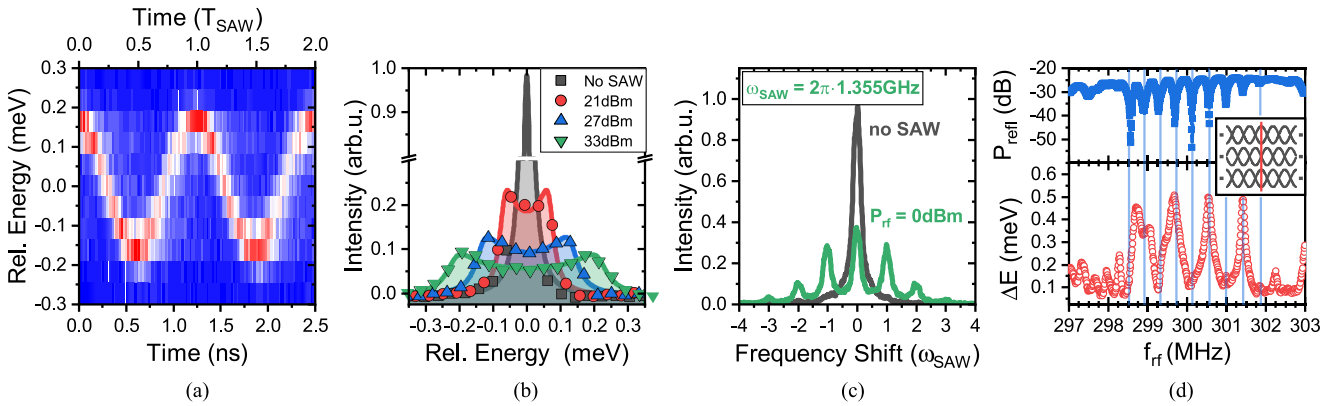

FIGURE 4. **(a) Time-resolved PL of a SAW-modulated QD exciton line, showing pure sinusoidal oscillations with a period equal to the SAW drive period. (b) Time-integrated PL of a SAW-modulated QD exciton, showing clear modulation with increasing SAW power consistent with deformation-potential coupling. (c) QD exciton resonance fluorescence showing several optomechanical sidebands at multiples of the SAW drive frequency. (d) Top: Reflected power spectrum of IDTs driving a SAW resonator with embedded QDs in a hybrid GaAs-$LiNbO_3$ system. Bottom: Modulation amplitude as a function of the IDT frequency, showing pronounced enhancement at the SAW cavity resonances.**

QDs in a ZnTe substrate using a ZnO layer to excite a SAW on the otherwise weakly-piezoelectric substrate [74]. This dynamic modulation can be observed by either time domain or stroboscopic-excitation spectroscopy. Fig. 4(a) shows the time- and energy-dependent photoluminescence (PL) emission from a single acoustically modulated QD exciton over the course of two acoustic cycles. The QD was modulated at a frequency of $f_{SAW} = 800$ MHz and was optically excited by a continuous wave (CW) laser. The collected emission from the QD transition was spectrally filtered and analyzed in the time domain by time-correlated single-photon counting. The measured data nicely shows the sinusoidal modulation of the QD emission, where the modulation frequency corresponds to that of the driving acoustic field. The modulation amplitude, in this case, $\Delta E = 0.156$ meV, is a measure of the hydrostatic pressure at the position of the QD, which corresponds to ≈ 1 MPa. For more detailed information about stroboscopic-excitation spectroscopy and the other PL experiments in this section, the reader is referred to [25] and [109].

The QD modulation amplitude ΔE can also be obtained from time-integrated spectra, as shown in Fig. 4(b). Here, time-integrated spectra are shown for different radio-frequency (RF) powers P_{RF} that are applied to the IDT and thus for different SAW amplitudes u_z. The initial Lorentzian line shape of the unmodulated QD exciton emission is broadened under the influence of the SAW, and a characteristic split spectrum emerges once the modulation amplitude exceeds the spectral width of the emission line. For increasing P_{RF}, an increase in the broadening and the modulation amplitude ΔE is observed. The modulation amplitude's scaling with the applied RF-power P_{RF} is determined by the physics of the QD spectral modulation. For modulation mediated via the deformation potential of the QD, $\Delta E \propto \sqrt{P_{RF}}$, because both the SAW amplitude u_z and the hydrostatic strain amplitude ϵ_{max} are proportional to $\sqrt{P_{RF}}$. The QD modulation amplitude may also increase via the quantum confined Stark effect, where the electric field associated with a SAW propagating in a piezoelectric substrate modulates the QD: $\Delta E \propto P_{RF}$ [85], [110]. In Fig. 4(b), the power dependence of the observed modulation agrees with $\Delta E \propto \sqrt{P_{RF}}$, indicating deformation potential coupling is the dominant contribution to the QD spectral modulation.

Compared to nonresonant excitation used for PL spectroscopy, resonant excitation of a specific transition in a single semiconductor QD greatly enhances the quality of the emitted photons in terms of purity and indistinguishability, as they adapt to the coherence of the driving laser field while maintaining their single photon characteristics. Combined with a dynamic modulation by a SAW, this makes it possible to advance into the resolved-sideband regime, meaning the SAW-induced spectral modulation frequency exceeds the optical linewidth. Fig. 4(c) shows the resonance fluorescence signal of a single QD transition with (green) and without (gray) dynamic modulation by a SAW. When the QD is not modulated by the SAW, the spectrum consists of a single emission line, the so-called zero phonon line (ZPL), with a linewidth limited by either the linewidth of the detection system or the driving resonant light field [33]. For the case of a dynamically modulated QD, the spectrum shows additional sidebands on either side of the ZPL. The splitting of the sidebands corresponds to the energy $\hbar\omega_{SAW}$ of a single SAW phonon. The formation of these phononic sidebands was first shown by Metcalfe et al. [3] for QDs in a planar Bragg cavity and by Villa et al. [111] for QDs in a pillar microcavity.

Extending this excitation scheme to an additional SAW field with a different frequency, both sum and difference frequencies are observed in the emission spectra, probing optomechanical wave mixing of two SAW fields and the driving CW laser field by the QD [5]. In the case of two mutually coherent SAW fields, the sum and difference SAW frequency generation processes depend on the phase between the two fields and a phase-matching scheme can be applied to control the relative intensity of specific sidebands. Furthermore, it could be shown that the different phononic sidebands show

IEEE Transactions on Quantum Engineering

pronounced temporal dynamics that can be controlled by detuning the driving laser from resonance, paving the way toward precise temporal and spectral control of single-photon emission [109]. The experiments presented so far are also compatible with a multitude of different photonic systems. For instance, the dynamic strain field of a SAW was used to control QDs in photonic cavities, enabling the realization of a triggered single-photon source [112], or QDs located in the input waveguide of a dynamically tuned Mach–Zehnder interferometer, enabling wavelength division multiplexing of single photons [113].

In order to enhance the coupling of QDs to the acoustic strain field, the QDs can be placed in nanomechanical structures and cavities designed to focus the strain fields at the position of the QDs, for example, nanophononic strings [114]. Focusing SAW cavities and IDT electrodes are also being investigated to enhance SAW interaction with QDs embedded in a GaAs substrate. Using focusing SAW cavities, Imany et al. [52] demonstrated resonance fluorescence of InAs QDs in the optomechanical resolved-sideband regime with a maximum single-phonon coupling rate of $g_0 = 2\pi \times 42$ kHz, which is expected to increase to $2\pi \times 10$ MHz with improved device design.

Instead of patterning SAW cavities around QDs in a weakly-piezoelectric host substrate, a different approach is to transfer QDs onto a strongly-piezoelectric substrate, i.e., $LiNbO_3$, allowing for the generation of stronger SAW fields with lower RF drive power. A key requirement for such a transfer is robust mechanical coupling across the interface between the host substrate containing the QDs and the target substrate used to generate the SAW. This has been realized for QDs and QD-like emission centers that are located within semiconductor nanowires (NW) [84], [85], [86]. Due to the stronger electromechanical coupling efficiency of $LiNbO_3$ and the associated stronger piezoelectric fields, spectral modulation of QD emission was observed due to both deformation potential coupling and the quantum confined Stark effect. Epitaxial lift-off and transfer of thin semiconductor membranes containing QDs have also been shown to be a successful technique for the fabrication of fused $LiNbO_3$–(Al)GaAs hybrid devices with enhanced acousto-optic coupling due to acoustic waveguiding and strong localization of the acoustic field within the transferred semiconductor membrane [63]. GaAs-based *p-i-n* photodiodes containing a single layer of QDs were successfully fabricated on $LiNbO_3$, enabling the combined dynamic and static tuning of the dot emission energy through the acoustic field of a SAW and a static electric field applied at the diode [115]. This technique can also be used to transfer the (Al)GaAs-QD membrane inside a SAW resonator patterned on $LiNbO_3$ [25]. High acoustic quality factors $Q > 2500$ are demonstrated for an operation frequency of $f = 300$ MHz even after the heterointegration of the semiconductor QD membrane, which ensures the coherent behavior of the SAW field. The optomechanical response of the QD presented in Fig. 4(d) with the simultaneously measured electrical spectrum of the resonator proves the efficient coupling of the QD to the resonator modes. The optomechanical coupling has an index-dependent character due to the position of the QD in the SAW cavity [see the inset of Fig. 4(d)]. The QD emission's frequency-dependent response shows complex behavior, with the presence of frequency-mixed peaks on the lower end of the frequency spectrum occurring between the phononic modes in the optomechanical response. To understand this possible nonlinear frequency conversion in the SAW resonator-QD coupling, resonators with higher resonant frequencies can be used to reach the resolved sideband regime [3]. In this regime, the contribution of each phonon interaction can be identified in the emission spectrum and the frequency mixing can be confirmed [5].

B. SAW–SPIN COUPLING IN DEFECT CENTERS

Optically-addressable solid-state spins are widely investigated resources in quantum information science and technology [116], [117], with myriad applications in quantum communication, networking [118], [119], and sensing [120], [121]. Bound solid-state electronic spins may be realized either through local electrostatic potentials or via impurities in a host semiconductor crystal. A canonical example is a point defect in a wide-bandgap material such as diamond or silicon carbide (SiC), which we focus on in this review. Atomic-scale defects feature electronic localization as well as distinct spin and optical transitions that can be individually and coherently addressed. These defect-based spin centers can be integrated with photonic [116], [122], [123], [124] and phononic systems, including SAW transducers and resonators. SAWs can manipulate not only the defect's optical and charge degrees of freedom, but they can also directly manipulate spins through their resonant interaction with the fine-structure splitting as discussed in Section II-D. Acoustic control offers an additional degree of freedom for both coherent sensing [11], [125] and accessing novel regimes of spin–phonon interaction [126]. Commonly used experimental tools of the field include ODMR, Ramsey interferometry, and spin-echo and dynamical decoupling microwave control, respectively, used to read out spin states, probe spin coherence, and to not only isolate but also coherently control interactions with neighboring systems [23], [127], [128].

1) NV CENTERS IN DIAMOND

The NV center in diamond is an extremely sensitive probe of its local environment, motivating extensive research into using NV centers as a nanoscale magnetic field [129], [130], [131], [132], electric field [133], [134], [135], [136], temperature [137], [138], pressure [139], and stress and strain [140] sensor operable at room temperature [126], [128], [141], [142]. The NV center features high-coherence spin states and a bright optical transition coupled to a spin-selective nonradiative transition that enables high-fidelity optical spin initialization and readout.

Golter et al. [9] coupled single-NV centers to propagating SAWs, demonstrating acoustic control of the NV orbital

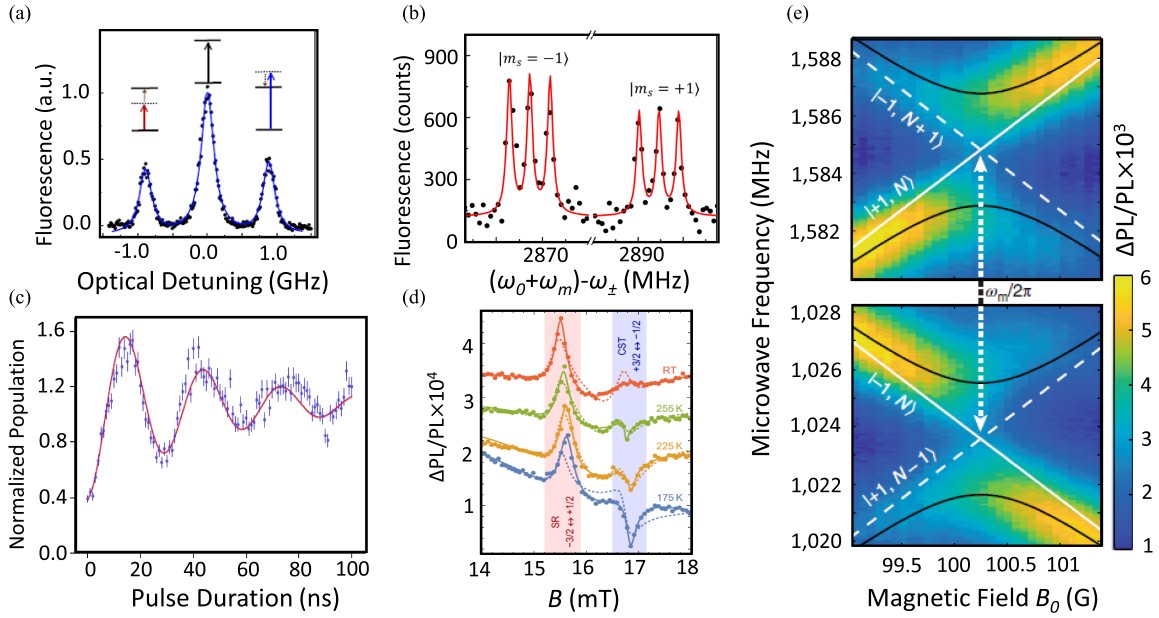

FIGURE 5. (a) Resonance fluorescence of the NV$^-$ center in diamond showing red and blue-detuned optomechanical sidebands from SAW driving. (b) Effective spin–spin interactions between the $m_s=\pm1$ and $m_s=0$ states driven by optomechanical sideband transitions. (c) Diamond SiV$^-$ center spin Rabi rotations driven by SAWs. (d) ODMR spectrum of V_{Si} centers in 4H-SiC with signatures of acoustic spin resonance (red banner) and coherent spin trapping (blue banner). (e) ODMR spectrum showing Autler–Townes splittings of VV^0 centers in 4H-SiC, the avoided crossings of hybridized spin–phonon modes as a magnetic field is tuned through the SAW resonator resonance. Figures reproduced with permission from (a) [9], (b) [75], (c) [76] (d) [11], and (e) [10].

state in the optomechanical resolved-sideband regime—a step toward quantum control of hybrid atom-phonon systems. Fig. 5(a) shows the NV$^-$ center driven by a SAW field at $\omega_m = 2\pi \times 900$ MHz as an optical pump is swept over the $|m_s=0\rangle$ to $|E_y\rangle$ optical transition at 637 nm, showing clear optomechanical sidebands detuned from the direct dipole-optical transition by ω_m. The authors also demonstrated optomechanically driven Rabi oscillations with Rabi frequencies exceeding 60 MHz, aided by the large strain susceptibility of the NVs excited states [9].

While the NV optical transition can be parametrically driven by SAWs, the NV ground state spin couples to strain with a susceptibility about six orders of magnitude weaker than the NV excited states [143], [144], necessitating alternative approaches to effectively couple the ground state spin to SAWs. By contrast, the excited states of the NV center have a relatively strong strain susceptibility facilitated by an orbital deformation potential of 6.1 THz/% [145], though they decay quickly to the ground state due to optical transitions. Instead, large spin–phonon interactions with the NV ground state can be engineered using a Raman scattering scheme where SAW phonons assist in driving transitions of a spectrally-isolated Λ-type three-level system comprising the $m_s=0$ ground state, the $m_s=\pm1$ ground state, and the E_y excited state. The excited-state population can be made negligible by either (1) tuning the resonant optical and acoustic drive amplitudes to realize a dark state, or (2) employing an off-resonant Raman transition, resulting in an effective spin–spin interaction. Using these techniques, Golter et al. [75] realized coherent spin–SAW phonon interactions in both time-resolved and spectral-domain experiments.

Fig. 5(b) shows a PL spectrum where SAW-assisted transitions from the $m_s=\pm1$ states are selectively addressed using the $|m_s=0\rangle - |m_s=\pm1\rangle$ NV$^-$ center zero-field splitting at 2.88 GHz. The three well-resolved peaks for each $m_s=\pm1$ spin state correspond to hyperfine splittings of 2.2 MHz from the nitrogen $I=1$ nuclear spin. Such nuclear spin-dependent transitions indicate the potential for accessing nuclear spins in SAW quantum acoustics. The transition resonance linewidths of 0.7 MHz agree with predictions from the spin dephasing rate dominated by the nuclear spin bath, suggesting no additional inhomogeneous broadening from the optical and SAW drives. An effective $|m_s=0\rangle - |m_s=\pm1\rangle$ spin–spin interaction rate of $2\pi \times 0.3$ MHz was extracted by varying the duration of the optical drive pulse, and by analyzing the dependence of the interaction and decay rates on the detuning of the SAW and optical excitation, the authors show the potential for strong spin–phonon coupling with ultralow optical pump power and negligible added spin dephasing [75].

2) SILICON VACANCY CENTERS IN DIAMOND

The negatively-charged silicon-vacancy (SiV$^-$) center in diamond has emerged as an attractive spin–photon interface for quantum networking applications, with a Debye–Waller factor of 0.75 and a ZPL transition compatible with down-conversion to the telecommunications C-band [146], [147].

The SiV^- center also features high mechanical susceptibilities for its spin transitions on the order of 10 THz/% [32] while still operating as a long-lived spin qubit with a coherence time greater than 10 ms at millikelvin temperatures [148]. This sensitive spin–phonon coupling could enable SAW-SiV^- devices to reach the strong-coupling regime with feasible mechanical quality factors of $Q \approx 10^3$ [32].

Recently, Maity et al. demonstrated SAW coherent control of both the SiV^- center electronic spin [76] as well as a single ^{13}C nuclear spin neighboring an SiV center [23]. IDTs with a 3.43-GHz center frequency resonant with a single SiV^- spin drove Rabi oscillations with a Rabi frequency of (34.0 ± 0.2) MHz [see Fig. 5(c)]. The SiV^- was initialized and read out optically via optical pumping and fluorescence from a Λ-type three-level system, where the spin qubit levels were coupled to an orbital excited state via one spin-preserving and one spin-flipping optical transition. Using focusing IDTs enhanced the SiV^- driving efficiency, reducing the required SAW power to between 3 and 350 μW [76], which is promising for operation at millikelvin temperatures to preserve high-spin coherence times. The mechanically-driven oscillations of the SiV electronic spin state were then used to control a ^{13}C nuclear spin [23]. The ^{13}C nuclear spin resonance was identified by applying a dynamical decoupling sequence to the IDTs, where periodic dips in the fluorescence from the SiV^- for a pulse separation of 1.578 μs indicated a weakly-coupled spin interacting coherently with the SiV^-. The spin could also be selectively initialized, read out, and driven, with fidelities ≈ 0.9 limited by the unintentional partial addressing of other ^{13}C nuclear spins, which may be reduced with longer pulse separation times [23]. These experiments demonstrate nuclear spin control similar to microwave-based experiments with the NV center in diamond [149], [150], [151] with orders of magnitude lower on-chip power.

3) DEFECT CENTERS IN SILICON CARBIDE

Benefiting from a mature semiconductor processing industry, SiC is available in 4-in wafers of isotopically-purified material, enabling long spin coherence times, and it is commercially available in thin films with robust processing methods [116]. It is no surprise, then, that several optically addressable defect centers have been explored in SiC, including several vacancy, divacancy, and antisite intrinsic defects of silicon and carbon, as well as many extrinsic defects [152]. While exploring novel candidates defect centers is an active research area, the silicon-vacancy (V_{Si}) and neutral divacancy (V_{Si} V_C) defects in the 4H-SiC polytype have demonstrated isolated single-photon emission and millisecond-long spin coherence times, critical milestones for practical quantum applications [116].

Shortly after their discovery, researchers began investigating these defects' susceptibilities to strain [127] and coupling them to SAWs. Leveraging the $S = 3/2$ spin manifolds of both ground and excited states of the V_{Si} center, Hernández-Mínguez et al. [77] demonstrated spin acoustic resonance with control over $\Delta m_s = \pm 1$ and $\Delta m_s = \pm 2$ transitions in both the ground and excited states with tuning provided by a static magnetic field. Hernández-Mínguez et al. later showed that the V_{Si} center can be continuously optically driven while preserving the spin quantization along a predefined spin precession axis. A single-SAW drive detuned from both the ground and excited state spin splittings is used to align the Rabi precession axes of the ground and excited-state spins, maintaining the spin projection along the precession axis for times limited only by intrinsic spin relaxation [11] [see Fig. 5(d)].

Using a SAW resonator with focusing Bragg reflectors, Whiteley et al. demonstrated strong spin–SAW phonon coupling with spins in V_{Si} V_C defects of 4H-SiC. The V_{Si} V_C ensemble spin manifold with $S = 1$ was controlled by both an IDT, which drove the SAW cavity housing the spins, and a static magnetic field, which tuned the $|m_s = -1\rangle - |m_s = +1\rangle$ Zeeman splitting to selectively address both $\Delta m_s = \pm 1$ and $\Delta m_s = \pm 2$ transitions. Acoustic paramagnetic resonance for both the *hh* and *kk* configurations of the V_{Si} V_C defects was measured over the profile of the SAW resonator, which confirmed the purely mechanical driving of the $\Delta m_s = \pm 1$ spin transitions. For the magnetic dipole-forbidden $\Delta m_s = \pm 2$ transition, the authors observed an acoustically-driven Rabi frequency of 1.1 MHz at 25 mW applied RF power to the SAW cavity. The Autler–Townes effect was also measured via the splitting of the $|m_s = -1\rangle$ state as the $\Delta m_s = \pm 2$ transition was tuned into resonance with the SAW cavity, showing hybridization of the spin state and SAW field [see Fig. 5(e)] [10].

C. DEFECTS IN LAYERED VAN DER WAALS MATERIALS

Within the last decade, many two-dimensional van der Waals layered materials (2DM) such as insulating hBN [153], [154], [155] and semiconducting transition metal dichalcogenides (TMDCs) [156], [157], [158], [159], [160] have emerged as promising platforms for nonclassical light emission [161], [162]. What is particularly appealing about quantum emitters in 2DMs is their high sensitivity to strain, motivating extensive research into mechanically controlled single-photon emission [162], [163]. In this section, we focus on experiments with defects in hBN due to the limited literature available for other 2DM coupled to SAWs. Although PL spectra of SPEs in TMDCs show acoustic phonon sidebands [162], [164] and exhibit spectral shifts when static strain is applied [165], [166], emitters in these materials have not yet been interfaced with SAWs; however, the experiments described below on hBN suggest an efficient coupling with SAWs should be possible for TMDCs and other 2DMs and that comparable effects to those observed in QDs and color center systems can be expected.

The atomistic deep-level defects in hBN flakes [167], [168], [169], powder [170], and epitaxially grown films [171] have appeared as room-temperature single-photon emitters [105], [155], [172] with transform-limited linewidths as

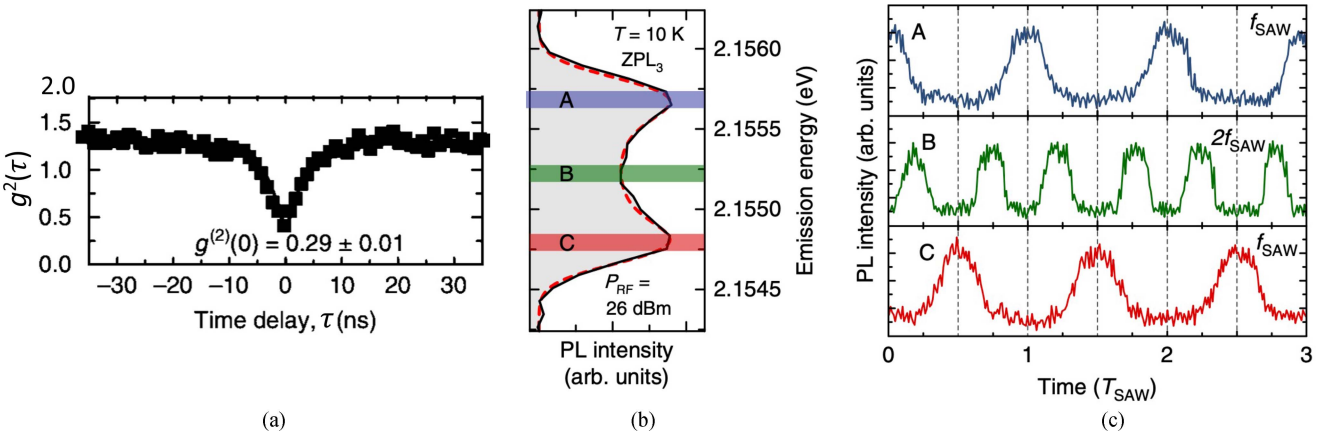

FIGURE 6. **(a) Normalized second-order correlation function $g^{(2)}(\tau)$ of an hBN spectral line illustrating photon antibunching. (b) Time-averaged PL spectrum. The dashed red line designates a fit, and the three color-coded rectangles (labeled A, B, C) mark the energy regions used for spectral filtering. (c) All three traces represent the time-dependent emission intensity spectrally filtered at the three color-coded energy regions indicated in (b) as A, B, and C. Figures reproduced/adapted with permission (CCBY 4.0) [16].**

narrow as ≈ 50 MHz at cryogenic temperatures [35]. Various hBN defects exhibit photon antibunching when measuring the normalized second-order correlation function $g^{(2)}(\tau)$ at zero time delay, $\tau = 0$ [see Fig. 6(a)] [16], [168], a characteristic signature of single-photon emission behavior [172]. In polarization-resolved micro-PL (μ-PL) measurements, the emission by hBN defects is highly linearly polarized, originating from the anisotropic structure of the emission center [16], [153], [173].

Recent experiments have demonstrated that defects in hBN are highly sensitive to strain, observed in both static and dynamic tuning of nonclassical light emission. Initial studies tuned emission from defects in hBN using static electric [174] and strain fields [167], [168], [175], the latter producing shifts of roughly 1–13 meV/%. SAWs were then investigated for dynamic, time-dependent strain tuning of defects in hBN. SAWs couple to defects in hBN primarily through the hBN deformation potential, with a mechanical susceptibility of 50 meV/% or approximately 10 THz/% [16]; on piezoelectric substrates, they may also couple via the electric field of piezoelectric SAWs, which induces a Stark effect [176]. Nonresonant PL spectroscopy of hBN defects modulated by traveling-wave SAWs exhibit lineshape broadening and split resonances with amplitudes up to 2.5 meV [15], [16]. Fig. 6(b) and (c) shows an exemplary split resonance with time-binning of the emission windows labeled A, B, C exhibiting clear oscillations at either the SAW frequency (A, C) or twice the SAW frequency (B), consistent with a time-modulated Lorentzian lineshape. Lazić et al. [16] showed that the contribution of the SAWs piezoelectric field is independent of its orientation with respect to the defect's symmetry axis and, therefore, can be neglected in comparison to the acousto-mechanical effect mediated through the defect deformation potential.

The large strain susceptibility demonstrated in hBN defects motivates future work integrating hBN defects as well as other 2DM with SAWs. One promising direction is integrating hBN defects into SAW resonators, moving the field into Stage 2 (cf. Table 1) and potentially enabling studies of coherent SAW–artificial atom interactions at room temperature. To successfully integrate hBN defects into SAW resonators, the hBN defects must be placed into robust mechanical contact with the SAW substrate. Existing approaches have relied on transferred hBN flakes [15] or powder grains [16], which have nonuniform physical contact with the SAW substrate. Due to the weak interlayer van der Waals mechanical coupling, SAW strain is not efficiently transferred to defects at the top of a multilayer flake or other 2-D structure [15], thus limiting the yield of optically bright emitters coupled to SAWs. Tackling this challenge will open new possibilities for room-temperature single-photon emission, including frequency modulation and spectral stabilization of individual photons.

IV. CONCLUSION AND OUTLOOK

Examining the different stages of development introduced in Table 1, the state-of-the-art SAW control is in Stage 2—resonant classical control—for both semiconductor QD excitons and optically-addressable spins, with numerous demonstrations in Stage 1. Experiments with QDs show the SAW-QD optomechanical interaction in both the time and frequency domains, with observations of multiple phononic sidebands, including sum and difference frequency mixing [5], as well as resonant enhancement of the exciton SAW modulation amplitude [25]. Semiconductor defect centers have demonstrated control by SAWs not only in the orbital but also the electronic and nuclear spin degrees of freedom [9], [23], [77], with demonstrations of mode hybridization and Rabi oscillations indicating that large couplings to SAWs can be achieved [10]. The recent integration of SAWs with defects in hBN [16] shows promising results for dynamic strain tuning of single-photon emitters operating at

room temperature. For all SAW–artificial atom platforms, movement toward Stage 3 will be facilitated by acoustic cavities with greater quality factors [17], enhanced atom and spin–phonon interaction via localized SAW modes [38], [52], and impedance-matched SAW transducers for efficient acoustic excitation and detection [60].

In addition to the optically-active systems explored in this review, the study of SAWs coupled to electrically-active quantum emitters is rapidly evolving. Several milestone experiments have been demonstrated within the last five years, including SAW Fock-state generation [27], strong multimode interactions and squeezing [13], [28], an acoustic analog of Young's double-slit experiment [14], as well as quantum state transfer and remote entanglement [39]. Large capacitive and inductive couplings ≈10 MHz are realized by appreciable spatial overlaps between the SAW mode and a qubit, which may be coupled to SAWs via an IDT [13], [27] or integrated within the SAW mirrors [28]. The large couplings enabled these systems to reach Stage 3 in Table 1. Electrostatic QDs are another electrically active system that couples to SAWs; such systems were investigated theoretically in [17] and recently demonstrated coherent SAW spin control and transport [8].

Strong coherent interactions can be engineered in both electromechanical and optomechanical SAW–artificial atom hybrid systems, suggesting the potential to integrate SAWs with both optically and electrically-active quantum emitters in a complete electro-optomechanical system. Such a hybrid system would enable the study of interactions between microwave quantum systems and single optical photons mediated through SAW mechanics. One can envision coupling microwave-frequency qubits and single-photon emitters through their mutual interactions with SAWs, providing a path toward microwave-optical entanglement and microwave-to-optical state transfer [17]. The platform-agnostic coupling of many quantum emitters to SAWs via strain, electric and magnetic fields enables many possible approaches to realizing complex microwave-SAW-optical hybrid quantum systems.

REFERENCES

[1] P. Delsing et al., "The 2019 surface acoustic waves roadmap," *J. Phys. D: Appl. Phys.*, vol. 52, no. 35, Aug. 2019, Art. no. 353001, doi: 10.1088/1361-6463/ab1b04.

[2] J. R. Gell et al., "Modulation of single quantum dot energy levels by a surface-acoustic-wave," *Appl. Phys. Lett.*, vol. 93, no. 8, Aug. 2008, Art. no. 81115, doi: 10.1063/1.2976135.

[3] M. Metcalfe, S. M. Carr, A. Muller, G. S. Solomon, and J. Lawall, "Resolved sideband emission of InAs/GaAs quantum dots strained by surface acoustic waves," *Phys. Rev. Lett.*, vol. 105, no. 3, Jul. 2010, Art. no. 37401, doi: 10.1103/PhysRevLett.105.037401.

[4] F. J. R. Schülein et al., "Fourier synthesis of radiofrequency nanomechanical pulses with different shapes," *Nature Nanotechnol.*, vol. 10, no. 6, pp. 512–516, Apr. 2015, doi: 10.1038/nnano.2015.72.

[5] M. Weiß et al., "Optomechanical wave mixing by a single quantum dot," *Optica*, vol. 8, no. 3, pp. 291–300, Mar. 2021, doi: 10.1364/OPTICA.412201.

[6] S. Hermelin et al., "Electrons surfing on a sound wave as a platform for quantum optics with flying electrons," *Nature*, vol. 477, no. 7365, pp. 435–438, Sep. 2011, doi: 10.1038/nature10416.

[7] R. P. G. McNeil et al., "On-demand single-electron transfer between distant quantum dots," *Nature*, vol. 477, no. 7365, pp. 439–42, Sep. 2011, doi: 10.1038/nature10444.

[8] B. Jadot et al., "Distant spin entanglement via fast and coherent electron shuttling," *Nature Nanotechnol.*, vol. 16, no. 5, pp. 570–575, May 2021, doi: 10.1038/s41565-021-00846-y.

[9] D. A. Golter, T. Oo, M. Amezcua, K. A. Stewart, and H. Wang, "Optomechanical quantum control of a nitrogen-vacancy center in diamond," *Phys. Rev. Lett.*, vol. 116, no. 14, Apr. 2016, Art. no. 143602. doi: 10.1103/PhysRevLett.116.143602.

[10] S. J. Whiteley et al., "Spin–phonon interactions in silicon carbide addressed by Gaussian acoustics," *Nature Phys.*, vol. 15, no. 5, pp. 490–495, May 2019, doi: 10.1038/s41567-019-0420-0.

[11] A. Hernández-Mínguez, A. V. Poshakinskiy, M. Hollenbach, P. V. Santos, and G. V. Astakhov, "Acoustically induced coherent spin trapping," *Sci. Adv.*, vol. 7, no. 44, Oct. 2021, Art. no. eabj5030, doi: 10.1126/sciadv.abj5030

[12] M. V. Gustafsson, T. Aref, A. F. Kockum, M. K. Ekstrom, G. Johansson, and P. Delsing, "Propagating phonons coupled to an artificial atom," *Science*, vol. 346, no. 6206, pp. 207–211, Oct. 2014, doi: 10.1126/science.1257219.

[13] B. A. Moores, L. R. Sletten, J. J. Viennot, and K. W. Lehnert, "Cavity quantum acoustic device in the multimode strong coupling regime," *Phys. Rev. Lett.*, vol. 120, no. 22, May 2018, Art. no. 227701. doi: 10.1103/PhysRevLett.120.227701

[14] L. R. Sletten, B. A. Moores, J. J. Viennot, and K. W. Lehnert, "Resolving phonon fock states in a multimode cavity with a double-slit qubit," *Phys. Rev. X*, vol. 9, no. 2, Jun. 2019, Art. no. 021056, doi: 10.1103/PhysRevX.9.021056.

[15] F. Iikawa et al., "Acoustically modulated optical emission of hexagonal boron nitride layers," *Appl. Phys. Lett.*, vol. 114, no. 17, Apr. 2019, Art. no. 171104, doi: 10.1063/1.5093299.

[16] S. Lazić et al., "Dynamically tuned non-classical light emission from atomic defects in hexagonal boron nitride," *Commun. Phys.*, vol. 2, no. 1, pp. 1–8, Dec. 2019, doi: 10.1038/s42005-019-0217-6.

[17] M. J. A. Schuetz, E. M. Kessler, G. Giedke, L. M. K. Vandersypen, M. D. Lukin, and J. I. Cirac, "Universal quantum transducers based on surface acoustic waves," *Phys. Rev. X*, vol. 5, no. 3, Sep. 2015, Art. no. 031031, doi: 10.1103/PhysRevX.5.031031.

[18] L. Wang et al., "High performance 33.7 GHz surface acoustic wave nanotransducers based on AlScN/diamond/Si layered structures," *Appl. Phys. Lett.*, vol. 113, no. 9, Aug. 2018, Art. no. 093503, doi: 10.1063/1.5046113.

[19] M. Weiß and H. J. Krenner, "Interfacing quantum emitters with propagating surface acoustic waves," *J. Phys. D: Appl. Phys*, vol. 51, no. 37, Sep. 2018, Art. no. 373001, doi: 10.1088/1361-6463/aace3c.

[20] R. Manenti, M. J. Peterer, A. Nersisyan, E. B. Magnusson, A. Patterson, and P. J. Leek, "Surface acoustic wave resonators in the quantum regime," *Phys. Rev. B*, vol. 93, no. 4, Jan. 2016, Art. no. 041411, doi: 10.1103/PhysRevB.93.041411.

[21] T. Aref et al., "Quantum acoustics with surface acoustic waves," in *Superconducting Devices in Quantum Optics*. Cham, Switzerland: Springer, 2016, pp. 217–244, doi: 10.1007/978-3-319-24091-6_9.

[22] A. A. Clerk, K. W. Lehnert, P. Bertet, J. R. Petta, and Y. Nakamura, "Hybrid quantum systems with circuit quantum electrodynamics," *Nature Phys.*, vol. 16, no. 3, pp. 257–267, Mar. 2020, doi: 10.1038/s41567-020-0797-9.

[23] S. Maity et al., "Mechanical control of a single nuclear spin," *Phys. Rev. X*, vol. 12, Mar. 2022, Art. no. 011056, doi: 10.1103/PhysRevX.12.011056.

[24] A. N. Bolgar et al., "Quantum regime of a two-dimensional phonon cavity," *Phys. Rev. Lett.*, vol. 120, no. 22, May 2018, Art. no. 223603. doi: 10.1103/PhysRevLett.120.223603.

[25] E. D. S. Nysten, A. Rastelli, and H. J. Krenner, "A hybrid (Al)GaAs-$LiNbO_3$ surface acoustic wave resonator for cavity quantum dot optomechanics," *Appl. Phys. Lett.*, vol. 117, no. 12, Sep. 2020, Art. no. 121106, doi: 10.1063/5.0022542.

[26] R. Manenti et al., "Circuit quantum acoustodynamics with surface acoustic waves," *Nature Commun.*, vol. 8, no. 1, Oct. 2017, Art. no. 975, doi: 10.1038/s41467-017-01063-9.

[27] K. J. Satzinger et al., "Quantum control of surface acoustic-wave phonons," *Nature*, vol. 563, no. 7733, pp. 661–665, Nov. 2018, doi: 10.1038/s41586-018-0719-5.

[28] G. Andersson et al., "Squeezing and multimode entanglement of surface acoustic wave phonons," *PRX Quantum*, vol. 3, no. 1, Jan. 2022, Art. no. 010312, doi: 10.1103/PRXQuantum.3.010312.

[29] R. Riedinger et al., "Non-classical correlations between single photons and phonons from a mechanical oscillator," *Nature*, vol. 530, no. 7590, pp. 313–316, Feb. 2016, doi: 10.1038/nature16536.

[30] G. Khitrova, H. M. Gibbs, M. Kira, S. W. Koch, and A. Scherer, "Vacuum Rabi splitting in semiconductors," *Nature Phys.*, vol. 2, no. 2, pp. 81–90, Feb. 2006, doi: 10.1038/nphys227.

[31] B. V. Novikov et al., "Baric properties of InAs quantum dots," *Semiconductors*, vol. 42, pp. 1076–1083, 2008, doi: 10.1134/S1063782608090133.

[32] S. Meesala et al., "Strain engineering of the silicon-vacancy center in diamond," *Phys. Rev. B*, vol. 97, May 2018, Art. no. 205444, doi: 10.1103/PhysRevB.97.205444.

[33] C. Matthiesen, A. N. Vamivakas, and M. Atatüre, "Subnatural linewidth single photons from a quantum dot," *Phys. Rev. Lett.*, vol. 108, no. 9, Feb. 2012, Art. no. 093602, doi: 10.1103/PhysRevLett.108.093602.

[34] L. J. Rogers et al., "Multiple intrinsically identical single-photon emitters in the solid state," *Nature Commun.*, vol. 5, no. 1, Aug. 2014, Art. no. 4739, doi: 10.1038/ncomms5739.

[35] A. Dietrich et al., "Observation of Fourier transform limited lines in hexagonal boron nitride," *Phys. Rev. B*, vol. 98, no. 8, Aug. 2018, Art. no. 081414, doi: 10.1103/PhysRevB.98.081414

[36] D. L. T. Bell and R. C. M. Li, "Surface-acoustic-wave resonators," *Proc. IEEE*, vol. 64, no. 5, pp. 711–721, May 1976, doi: 10.1109/PROC.1976.10200.

[37] E. B. Magnusson et al., "Surface acoustic wave devices on bulk ZnO crystals at low temperature," *Appl. Phys. Lett.*, vol. 106, no. 6, Feb. 2015, Art. no. 063509, doi: 10.1063/1.4908248.

[38] L. Shao et al., "Phononic band structure engineering for high-Q gigahertz surface acoustic wave resonators on lithium niobate," *Phys. Rev. Appl.*, vol. 12, no. 1, Jul. 2019, Art. no. 014022, doi: 10.1103/PhysRevApplied.12.014022.

[39] A. Bienfait et al., "Phonon-mediated quantum state transfer and remote qubit entanglement," *Science*, vol. 364, no. 6438, pp. 368–371, Apr. 2019, doi: 10.1126/science.aaw8415.

[40] D. Morgan, *Surface Acoustic Wave Filters With Applications to Electronic Communications and Signal Processing*. Amsterdam, The Netherlands: Elsevier Science, 2007.

[41] T. P. Cameron and W. D. Hunt, "Reflection characteristics of obliquely incident surface acoustic waves from groove and aluminum gratings on 100-cut gallium arsenide," *J. Appl. Phys.*, vol. 84, no. 4, pp. 2212–2218, 1998, doi: 10.1063/1.368285.

[42] R. C. M. Li and J. A. Alusow, "Suppression of bulk-scattering loss at saw-resonator reflectors," *Electron. Lett.*, vol. 13, no. 19, pp. 580–581, Sep. 1977, doi: 10.1049/el:19770414.

[43] O. Painter, K. Srinivasan, and P. E. Barclay, "Wannier-like equation for the resonant cavity modes of locally perturbed photonic crystals," *Phys. Rev. B*, vol. 68, no. 3, Jul. 2003, Art. no. 035214, doi: 10.1103/PhysRevB.68.035214.

[44] J. Pedrós et al., "Guided propagation of surface acoustic waves and piezoelectric field enhancement in ZnO/GaAs systems," *J. Appl. Phys.*, vol. 110, no. 10, Art. no. 103501, doi: 10.1063/1.3660215.

[45] Y. Kim, W. D. Hunt, F. S. Hickernell, and R. J. Higgins, "Surface acoustic wave properties of ZnO films on {001}-cut< 110 >-propagating GaAs substrates," *J. Appl. Phys.*, vol. 75, no. 11, pp. 7299–7303, Jun. 1994, doi: 10.1063/1.356639.

[46] Y. Takagaki, P. Santos, E. Wiebicke, O. Brandt, H.-P. Schönherr, and K. Ploog, "Guided propagation of surface acoustic waves in AlN and GaN films grown on 4H–SiC (0001) substrates," *Phys. Rev. B*, vol. 66, no. 15, Oct. 2002, Art. no. 155439, doi: 10.1103/PhysRevB.66.155439.

[47] M. K. Ekström et al., "Towards phonon routing: controlling propagating acoustic waves in the quantum regime," *New J. Phys.*, vol. 21, no. 12, Dec. 2019, Art. no. 123013, doi: 10.1088/1367-2630/ab5ca5.

[48] V. W. L. Chin, T. L. Tansley, and T. Osotchan, "Electron mobilities in gallium, indium, and aluminum nitrides," *J. Appl. Phys.*, vol. 75, no. 11, pp. 7365–7372, 1994, doi: 10.1063/1.356650.

[49] M. M. de Lima, F. Alsina, W. Seidel, and P. V. Santos, "Focusing of surface-acoustic-wave fields on (100) GaAs surfaces," *J. Appl. Phys.*, vol. 94, no. 12, Dec. 2003, Art. no. 7848, doi: 10.1063/1.1625419.

[50] A. Bienfait et al., "Quantum erasure using entangled surface acoustic phonons," *Phys. Rev. X*, vol. 10, no. 2, Jun. 2020, Art. no. 021055, doi: 10.1103/PhysRevX.10.021055.

[51] M. E. Msall and P. V. Santos, "Focusing surface-acoustic-wave microcavities on GaAs," *Phys. Rev. Appl.*, vol. 13, no. 1, Jan. 2020, Art. no. 014037, doi: 10.1103/PhysRevApplied.13.014037.

[52] P. Imany et al., "Quantum phase modulation with acoustic cavities and quantum dots," *Optica*, vol. 9, no. 5, pp. 501–504, Apr. 2022, doi: 10.1364/OPTICA.451418.

[53] V. Laude, D. Gérard, N. Khelfaoui, C. F. Jerez-Hanckes, S. Benchabane, and A. Khelif, "Subwavelength focusing of surface acoustic waves generated by an annular interdigital transducer," *Appl. Phys. Lett.*, vol. 92, no. 9, Mar. 2008, Art. no. 094104, doi: 10.1063/1.2891055.

[54] A. Okada et al., "Cavity enhancement of anti-stokes scattering via optomechanical coupling with surface acoustic waves," *Phys. Rev. Appl.*, vol. 10, Aug. 2018, Art. no. 024002, doi: 10.1103/PhysRevApplied.10.024002.

[55] M. M. de Lima, Jr., J. Camacho, W. Seidel, H. Kostial, and P. V. Santos, "Intense acoustic beams for photonic modulation," *Photon. Crys. Mater. Nanostruct.*, vol. 5450, pp. 118–125, Sep. 2004, doi: 10.1117/12.545590.

[56] S. Benchabane, A. Khelif, J.-Y. Rauch, L. Robert, and V. Laude, "Evidence for complete surface wave band gap in a piezoelectric phononic crystal," *Phys. Rev. E*, vol. 73, no. 6, Jun. 2006, Art. no. 065601, doi: 10.1103/PhysRevE.73.065601.

[57] D. Yudistira, Y. Pennec, B. D. Rouhani, S. Dupont, and V. Laude, "Nonradiative complete surface acoustic wave bandgap for finite-depth holey phononic crystal in lithium niobate," *Appl. Phys. Lett.*, vol. 100, no. 6, Feb. 2012, Art. no. 061912, doi: 10.1063/1.3684839

[58] Y. He, J. Liu, C. Zhao, R. Huang, G. Dai, and W. Chen, "Control system of superconducting quantum computers," *J. Supercond. Novel Magn.*, vol. 35, no. 1, pp. 11–31, Jan. 2022, doi: 10.1007/s10948-021-06104-5.

[59] A. Winkler, R. Brünig, C. Faust, R. Weser, and H. Schmidt, "Towards efficient surface acoustic wave (SAW)-based microfluidic actuators," *Sens. Actuator A. Phys.*, vol. 247, pp. 259–268, Aug. 2016, doi: 10.1016/j.sna.2016.06.006.

[60] M. K. Ekström, T. Aref, J. Runeson, J. Björck, I. Boström, and P. Delsing, "Surface acoustic wave unidirectional transducers for quantum applications," *Appl. Phys. Lett.*, vol. 110, no. 7, Feb. 2017, Art. no. 073105, doi: 10.1063/1.4975803.

[61] K. Yamanouchi, H. Nakagawa, and H. Odagawa, "GHz-range surface acoustic wave low loss filter at super low temperature," in *Proc. IEEE Joint Meeting Eur. Freq. Time Forum Int. Freq. Control Symp.*, vol. 2, 1999, pp. 911–914, doi: 10.1109/FREQ.1999.841453.

[62] É. Dumur et al., "Unidirectional distributed acoustic reflection transducers for quantum applications," *Appl. Phys. Lett.*, vol. 114, Jun. 2019, Art. no. 223501, doi: 10.1063/1.5099095.

[63] E. D. S. Nysten, Y. H. Huo, H. Yu, G. F. Song, A. Rastelli, and H. J. Krenner, "Multi-harmonic quantum dot optomechanics in fused $LiNbO_3$-(Al)GaAs hybrids," *J. Phys. D: Appl. Phys.*, vol. 50, no. 43, Nov. 2017, Art. no. 43LT01, doi: 10.1088/1361-6463/aa861a.

[64] COMSOL Multiphysics, *Introduction to COMSOL Multiphysics*. Burlington, MA, USA: COMSOL Multiphysics, 1998. [Online]. Available: https://cdn.comsol.com/doc/5.5/IntroductionToCOMSOLMultiphysics.pdf

[65] U. C. Kaletta and C. Wenger, "FEM simulation of Rayleigh waves for CMOS compatible SAW devices based on AlN/SiO_2/Si(100)," *Ultrasonics*, vol. 54, no. 1, pp. 291–295, Jan. 2014, doi: 10.1016/j.ultras.2013.04.009.

[66] S. Fu et al., "High-frequency surface acoustic wave devices based on ZnO/SiC layered structure," *IEEE Electron Device Lett.*, vol. 40, no. 1, pp. 103–106, Jan. 2019, doi: 10.1109/LED.2018.2881467.

[67] D. Royer and E. Dieulesaint, *Elastic Waves in Solids II: Generation, Acousto-Optic Interaction, Applications*. Berlin, Germany: Springer, 1999.

[68] K. Hashimoto, T. Omori, and M. Yamaguchi, "Design considerations on surface acoustic wave resonators with significant internal reflection in interdigital transducers," *IEEE Trans. Ultrason., Ferroelect., Freq. Control*, vol. 51, no. 11, pp. 1394–1403, Nov. 2004, doi: 10.1109/TUFFC.2004.1367478.

[69] W. R. Smith, H. M. Gerard, J. H. Collins, T. M. Reeder, and H. J. Shaw, "Analysis of interdigital surface wave transducers by use of an equivalent circuit model," *IEEE Trans. Microw. Theory Techn.*, vol. TMTT-17, no. 11, pp. 856–864, Nov. 1969, doi: 10.1109/TMTT.1969.1127075.

[70] J. Larson, P. Bradley, S. Wartenberg, and R. Ruby, "Modified Butterworth-Van Dyke circuit for FBAR resonators and automated measurement system," in *Proc. IEEE Ultrason. Symp. Proc. Int. Symp. (Cat. No.00CH37121)*, 2000, vol. 1, pp. 863–868, doi: 10.1109/ULTSYM.2000.922679.

[71] P. Varshney et al., "Theoretical and experimental analysis of high Q SAW resonator transient response in a wireless sensor interrogation application," in *Proc. IEEE Int. Freq. Control Symp. Proc.*, Jul. 2012, pp. 1–6, doi: 10.1109/FCS.2012.6243714.

[72] E. Zeuthen, A. Schliesser, J. M. Taylor, and A. S. Sørensen, "Electrooptomechanical equivalent circuits for quantum transduction," *Phys. Rev. Appl.*, vol. 10, no. 4, Oct. 2018, Art. no. 044036, doi: 10.1103/PhysRevApplied.10.044036.

[73] M. Goryachev, N. Kostylev, and M. E. Tobar, "Single-photon level study of microwave properties of lithium niobate at millikelvin temperatures," *Phys. Rev. B*, vol. 92, no. 6, Aug. 2015, Art. no. 060406, doi: 10.1103/PhysRevB.92.060406.

[74] V. Tiwari et al., "Radio-frequency stress-induced modulation of CdTe/ZnTe quantum dots," *J. Appl. Phys.*, vol. 127, no. 23, Jun. 2020, Art. no. 234303, doi: 10.1063/5.0011124.

[75] D. A. Golter, T. Oo, M. Amezcua, I. Lekavicius, K. A. Stewart, and H. Wang, "Coupling a surface acoustic wave to an electron spin in diamond via a dark state," *Phys. Rev. X*, vol. 6, no. 4, Dec. 2016, Art. no. 041060, doi: 10.1103/PhysRevX.6.041060.

[76] S. Maity et al., "Coherent acoustic control of a single silicon vacancy spin in diamond," *Nature Commun.*, vol. 11, no. 1, Jan. 2020, Art. no. 193, doi: 10.1038/s41467-019-13822-x.

[77] A. Hernández-Mínguez, A. V. Poshakinskiy, M. Hollenbach, P. V. Santos, and G. V. Astakhov, "Anisotropic spin-acoustic resonance in silicon carbide at room temperature," *Phys. Rev. Lett.*, vol. 125, no. 10, Sep. 2020, Art. no. 107702, doi: 10.1103/PhysRevLett.125.107702.

[78] H. Nakahata et al., "SAW devices on diamond," in *Proc. IEEE Ultrason. Symp. Proc. Int. Symp.*, vol. 1, 1995, pp. 361–370, doi: 10.1109/ULTSYM.1995.495599.

[79] Y. Kim, W. Hunt, F. Hickernell, R. Higgins, and C.-K. Jen, "ZnO films on {001}-cut < 110 >-propagating GaAs substrates for surface acoustic wave device applications," *IEEE Trans. Ultrason., Ferroelect., Freq. Control*, vol. 42, no. 3, pp. 351–361, May 1995, doi: 10.1109/58.384443.

[80] S. Fujii et al., "Low propagation loss in a one-port SAW resonator fabricated on single-crystal diamond for super-high-frequency applications," *IEEE Trans. Ultrason., Ferroelect., Freq. Control*, vol. 60, no. 5, pp. 986–992, May 2013, doi: 10.1109/TUFFC.2013.2656.

[81] S. G. Bishop et al., "Room-temperature quantum emitter in aluminum nitride," *ACS Photon.*, vol. 7, no. 7, pp. 1636–1641, Jul. 2020, doi: 10.1021/acsphotonics.0c00528.

[82] S. Saravi, T. Pertsch, and F. Setzpfandt, "Lithium niobate on insulator: An emerging platform for integrated quantum photonics," *Adv. Opt. Mater.*, vol. 9, no. 22, Sep. 2021, Art. no. 2100789, doi: 10.1002/adom.202100789

[83] J.-H. Kim, S. Aghaeimeibodi, J. Carolan, D. Englund, and E. Waks, "Hybrid integration methods for on-chip quantum photonics," Optica, vol. 7, no. 4, pp. 291–308, 2020, doi: 10.1364/OPTICA.384118.

[84] A. Hernández-Mínguez et al., "Acoustically driven photon antibunching in nanowires," *Nano Lett.*, vol. 12, no. 1, pp. 252–258, Jan. 2012, doi: 10.1021/nl203461m.

[85] M. Weiß et al., "Dynamic acoustic control of individual optically active quantum dot-like emission centers in heterostructure nanowires," *Nano Lett.*, vol. 14, no. 5, pp. 2256–64, May 2014, doi: 10.1021/nl4040434.

[86] M. Weiß et al., "Radio frequency occupancy state control of a single nanowire quantum dot," *J. Phys. D: Appl. Phys*, vol. 47, no. 39, Oct. 2014, Art. no. 394011, doi: 10.1088/0022-3727/47/39/394011.

[87] F. M. Mayor, W. Jiang, C. J. Sarabalis, T. P. McKenna, J. D. Witmer, and A. H. Safavi-Naeini, "Gigahertz phononic integrated circuits on thin-film lithium niobate on sapphire," *Phys. Rev. Appl.*, vol. 15, no. 1, Jan. 2021, Art. no. 014039, doi: 10.1103/PhysRevApplied.15.014039.

[88] T. P. McKenna et al., "Cryogenic microwave-to-optical conversion using a triply resonant lithium-niobate-on-sapphire transducer," *Optica*, vol. 7, no. 12, pp. 1737–1745, Dec. 2020, doi: 10.1364/OPTICA.397235.

[89] G. Moody et al., "2022 roadmap on integrated quantum photonics," *J. Phys. Photon.*, vol. 4, no. 1, Jan. 2022, Art. no. 012501, doi: 10.1088/2515-7647/ac1ef4.

[90] G. D. Mahan, *Many-Particle Physics*. Berlin, Germany: Springer, 2013.

[91] I. Pelant and J. Valenta, *Luminescence Spectroscopy of Semiconductors* London, U.K.: OUP, 2012.

[92] A. Carmele and S. Reitzenstein, "Non-Markovian features in semiconductor quantum optics: Quantifying the role of phonons in experiment and theory," *Nanophotonics*, vol. 8, no. 5, pp. 655–683, Apr. 2019, doi: 10.1515/nanoph-2018-0222.

[93] V. M. Axt, M. Herbst, and T. Kuhn, "Coherent control of phonon quantum beats," *Superlattices Microstruct.*, vol. 26, no. 2, pp. 117–128, Aug. 1999, doi: 10.1006/spmi.1999.0765.

[94] A. Vagov, V. M. Axt, and T. Kuhn, "Electron-phonon dynamics in optically excited quantum dots: Exact solution for multiple ultrashort laser pulses," *Phys. Rev. B*, vol. 66, no. 16, Oct. 2002, Art. no. 165312, doi: 10.1103/PhysRevB.66.165312

[95] A. Vagov, M. D. Croitoru, M. Glässl, V. M. Axt, and T. Kuhn, "Real-time path integrals for quantum dots: Quantum dissipative dynamics with superohmic environment coupling," *Phys. Rev. B*, vol. 83, no. 9, Mar. 2011, Art. no. 0094303, doi: 10.1103/PhysRevB.83.094303.

[96] D. Reiter, D. Wigger, V. M. Axt, and T. Kuhn, "Generation and dynamics of phononic cat states after optical excitation of a quantum dot," *Phys. Rev. B*, vol. 84, no. 19, Nov. 2011, Art. no. 195327, doi: 10.1103/PhysRevB.84.195327

[97] T. Hahn, D. Groll, T. Kuhn, and D. Wigger, "Influence of excited state decay and dephasing on phonon quantum state preparation," *Phys. Rev. B*, vol. 100, no. 2, Jul. 2019, Art. no. 024306, doi: 10.1103/PhysRevB.100.024306

[98] D. Wigger, H. Gehring, V. M. Axt, D. E. Reiter, and T. Kuhn, "Quantum dynamics of optical phonons generated by optical excitation of a quantum dot," *J. Comput. Electron.*, vol. 15, no. 4, pp. 1158–1169, Jul. 2016, doi: 10.1007/s10825-016-0856-8.

[99] R. J. Glauber, "Coherent and incoherent states of the radiation field," *Phys. Rev.*, vol. 131, no. 6, Sep. 1963, Art. no. 2766, doi: 10.1103/PhysRev.131.2766

[100] D. Wigger, K. Gawarecki, and P. Machnikowski, "Remote phonon control of quantum dots and other artificial atoms," *Adv. Quantum Technol.*, vol. 4, no. 4, Apr. 2021, Art. no. 2000128, doi: 10.1002/qute.202000128.

[101] T. Hahn, D. Groll, H. J. Krenner, T. Kuhn, P. Machnikowski, and D. Wigger, "Photon scattering from a quantum acoustically modulated two-level system," *AVS Quantum Sci.*, vol. 4, Feb. 2022, Art. no. 011403, doi: 10.1116/5.0077024.

[102] P. Udvarhelyi, V. O. Shkolnikov, A. Gali, G. Burkard, and A. Pályi, "Spin-strain interaction in nitrogen-vacancy centers in diamond," *Phys. Rev. B*, vol. 98, no. 7, Aug. 2018, Art. no. 075201, doi: 10.1103/PhysRevB.98.075201.

[103] M. O. Scully and M. S. Zubairy, *Quantum Optics*. Cambridge, U.K.: Cambridge Univ. Press, 1999.

[104] M.-A. Lemonde et al., "Phonon networks with silicon-vacancy centers in diamond waveguides," *Phys. Rev. Lett.*, vol. 120, no. 21, May 2018, Art. no. 213603, doi: 10.1103/PhysRevLett.120.213603.

[105] I. Aharonovich, D. Englund, and M. Toth, "Solid-state single-photon emitters," *Nature Photon.*, vol. 10, no. 10, pp. 631–641, Oct. 2016, doi: 10.1038/nphoton.2016.186.

[106] R. Uppu, L. Midolo, X. Zhou, J. Carolan, and P. Lodahl, "Quantum-dot-based deterministic photon–emitter interfaces for scalable photonic quantum technology," *Nature Nanotechnol.*, vol. 16, 2021, Art. no. 1308–1317, doi: 10.1038/s41565-021-00965-6.

[107] T. Jakubczyk et al., "Impact of phonons on dephasing of individual excitons in deterministic quantum dot microlenses," *ACS Photon.*, vol. 3, no. 12, pp. 2461–2466, 2016, doi: 10.1021/acsphotonics.6b00707.

[108] T. Grange et al., "Reducing phonon-induced decoherence in solid-state single-photon sources with cavity quantum electrodynamics," *Phys. Rev. Lett.*, vol. 118, no. 25, Jun. 2017, Art. no. 253602, doi: 10.1103/PhysRevLett.118.253602.

[109] D. Wigger et al., "Resonance-fluorescence spectral dynamics of an acoustically modulated quantum dot," *Phys. Rev. Res.*, vol. 3, no. 3, Aug. 2021, Art. no. 033197, doi: 10.1103/PhysRevResearch.3.033197.

[110] S. Lazić, E. Chernysheva, Ž. Gačević, H. P. Van Der Meulen, E. Calleja, and J. M. Calleja Pardo, "Dynamic control of the optical emission from GaN/InGaN nanowire quantum dots by surface acoustic waves," *AIP Adv.*, vol. 5, no. 9, Sep. 2015, Art. no. 097217, doi: 10.1063/1.4932147.

[111] B. Villa et al., "Surface acoustic wave modulation of a coherently driven quantum dot in a pillar microcavity," *Appl. Phys. Lett.*, vol. 111, no. 1, Jul. 2017, Art. no. 011103, doi: 10.1063/1.4990966.

[112] M. Weiß et al., "Surface acoustic wave regulated single photon emission from a coupled quantum dot-nanocavity system," *Appl. Phys. Lett.*, vol. 109, no. 3, Jul. 2016, Art. no. 033105, doi: 10.1063/1.4959079.

[113] D. D. Bühler et al., "On-chip piezo-optomechanical dynamic single photon routing and rotation of a photonic qubit," 2022, *arXiv: 2202.10173*, doi: 10.48550/arXiv.2202.10173.

[114] A. Vogele et al., "Quantum dot optomechanics in suspended nanophononic strings," *Adv. Quantum Technol.*, vol. 3, no. 2, Feb. 2020, Art. no. 1900102, doi: 10.1002/qute.201900102.

[115] J. Pustiowski et al., "Independent dynamic acousto-mechanical and electrostatic control of individual quantum dots in a $LiNbO_3$-GaAs hybrid," *Appl. Phys. Lett.*, vol. 106, no. 1, Jan. 2015, Art. no. 013107, doi: 10.1063/1.4905477.

[116] D. D. Awschalom, R. Hanson, J. Wrachtrup, and B. B. Zhou, "Quantum technologies with optically interfaced solid-state spins," *Nature Photon.*, vol. 12, pp. 516–527, Sep. 2018, doi: 10.1038/s41566-018-0232-2.

[117] M. W. Doherty, C. R. Du, and G. D. Fuchs, "Quantum science and technology based on color centers with accessible spin," *J. Appl. Phys.*, vol. 131, no. 1, Jan. 2022, Art. no. 010401, doi: 10.1063/5.0082219.

[118] S.-H. Wei et al., "Towards real-world quantum networks: A review," *Laser Photon. Rev.*, vol. 16, no. 3, Jan. 2022, Art. no. 2100219, doi: 10.1002/lpor.202100219.

[119] M. Pompili et al., "Realization of a multinode quantum network of remote solid-state qubits," *Science*, vol. 372, no. 6539, pp. 259–264, Apr. 2021, doi: 10.1126/science.abg1919.

[120] A. J. Heinrich et al., "Quantum-coherent nanoscience," *Nature Nanotechnol.*, vol. 16, no. 12, pp. 1318–1329, Dec. 2021, doi: 10.1038/s41565-021-00994-1.

[121] C. Bradac, S. F. Lim, H.-C. Chang, and I. Aharonovich, "Optical nanoscale thermometry: From fundamental mechanisms to emerging practical applications," *Adv. Opt. Mater.*, vol. 8, no. 15, May 2020, Art. no. 2000183, doi: 10.1002/adom.202000183.

[122] C. T. Nguyen et al., "An integrated nanophotonic quantum register based on silicon-vacancy spins in diamond," *Phys. Rev. B*, vol. 100, Oct. 2019, Art. no. 165428, doi: 10.1103/PhysRevB.100.165428.

[123] H. Kraus et al., "Magnetic field and temperature sensing with atomic-scale spin defects in silicon carbide," *Sci. Rep.*, vol. 4, no. 1, Jul. 2014, Art. no. 5303, doi: 10.1038/srep05303.

[124] D. M. Lukin et al., "4H-silicon-carbide-on-insulator for integrated quantum and nonlinear photonics," *Nature Photon.*, vol. 14, no. 5, pp. 330–334, May 2020, doi: 10.1038/s41566-019-0556-6.

[125] E. R. MacQuarrie, T. A. Gosavi, A. M. Moehle, N. R. Jungwirth, S. A. Bhave, and G. D. Fuchs, "Coherent control of a nitrogen-vacancy center spin ensemble with a diamond mechanical resonator," *Optica*, vol. 2, no. 3, pp. 233–238, Mar. 2015, doi: 10.1364/OPTICA.2.000233.

[126] K. Kepesidis, S. Bennett, S. Portolan, M. Lukin, and P. Rabl, "Phonon cooling and lasing with nitrogen-vacancy centers in diamond," *Phys. Rev. B*, vol. 88, no. 6, Aug. 2013, Art. no. 064105, doi: 10.1103/PhysRevB.88.064105.

[127] A. L. Falk et al., "Electrically and mechanically tunable electron spins in silicon carbide color centers," *Phys. Rev. Lett.*, vol. 112, no. 18, May 2014, Art. no. 187601, doi: 10.1103/PhysRevLett.112.187601.

[128] D. Lee, K. W. Lee, J. V. Cady, P. Ovartchaiyapong, and A. C. B. Jayich, "Topical review: spins and mechanics in diamond," *J. Opt.*, vol. 19, no. 3, Feb. 2017, Art. no. 033001, doi: 10.1088/2040-8986/aa52cd.

[129] G. Balasubramanian et al., "Nanoscale imaging magnetometry with diamond spins under ambient conditions," *Nature*, vol. 455, no. 7213, pp. 648–651, Oct. 2008, doi: 10.1038/nature07278.

[130] L. Rondin, J.-P. Tetienne, T. Hingant, J.-F. Roch, P. Maletinsky, and V. Jacques, "Magnetometry with nitrogen-vacancy defects in diamond," *Rep. Prog. Phys.*, vol. 77, no. 5, May 2014, Art. no. 056503, doi: 10.1088/0034-4885/77/5/056503.

[131] T. Wolf et al., "Subpicotesla diamond magnetometry," *Phys. Rev. X*, vol. 5, Oct. 2015, Art. no. 041001, doi: 10.1103/PhysRevX.5.041001.

[132] J. Zhang et al., "Diamond nitrogen-vacancy center magnetometry: Advances and challenges," 2020, *arXiv: 2010.10231*, doi: 10.48550/arXiv.2010.10231.

[133] M. Block et al., "Optically enhanced electric field sensing using nitrogen-vacancy ensembles," *Phys. Rev. Appl.*, vol. 16, Aug. 2021, Art. no. 024024, doi: 10.1103/PhysRevApplied.16.024024.

[134] J. Michl et al., "Robust and accurate electric field sensing with solid state spin ensembles," *Nano Lett.*, vol. 19, no. 8, pp. 4904–4910, Jul. 2019, doi: 10.1021/acs.nanolett.9b00900.

[135] F. Dolde et al., "Nanoscale detection of a single fundamental charge in ambient conditions using the NV^- center in diamond," *Phys. Rev. Lett.*, vol. 112, Mar. 2014, Art. no. 097603, doi: 10.1103/PhysRevLett.112.097603.

[136] F. Dolde et al., "Electric-field sensing using single diamond spins," *Nature Phys.*, vol. 7, no. 6, pp. 459–463, Jun. 2011, doi: 10.1038/nphys1969.

[137] J. H. Shim et al., "Multiplexed sensing of magnetic field and temperature in real time using a nitrogen-vacancy ensemble in diamond," *Phys. Rev. Appl.*, vol. 17, Jan. 2022, Art. no. 014009, doi: 10.1103/PhysRevApplied.17.014009.

[138] S. Sotoma, C. P. Epperla, and H.-C. Chang, "Diamond nanothermometry," *ChemNanoMat*, vol. 4, no. 1, pp. 15–27, Oct. 2018, doi: 10.1002/cnma.201700257.

[139] K. O. Ho et al., "Probing local pressure environment in anvil cells with nitrogen-vacancy ($N\text{-}V^-$) centers in diamond," *Phys. Rev. Appl.*, vol. 13, Feb. 2020, Art. no. 024041, doi: 10.1103/PhysRevApplied.13.024041.

[140] M. S. J. Barson et al., "Nanomechanical sensing using spins in diamond," *Nano Lett.*, vol. 17, no. 3, pp. 1496–1503, Feb. 2017, doi: 10.1021/acs.nanolett.6b04544.

[141] L. Hall, J. Cole, C. Hill, and L. Hollenberg, "Sensing of fluctuating nanoscale magnetic fields using nitrogen-vacancy centers in diamond," *Phys. Rev. Lett.*, vol. 103, Apr. 2009, Art. no. 220802, doi: 10.1103/PhysRevLett.103.220802.

[142] S. Steinert et al., "High sensitivity magnetic imaging using an array of spins in diamond," *Rev. Sci. Instrum.*, vol. 81, no. 4, Apr. 2010, Art. no. 043705, doi: 10.1063/1.3385689.

[143] M. W. Doherty, N. B. Manson, P. Delaney, and L. C. L. Hollenberg, "The negatively charged nitrogen-vacancy centre in diamond: The electronic solution," *New J. Phys.*, vol. 13, no. 2, Feb. 2011, Art. no. 025019, doi: 10.1088/1367-2630/13/2/025019.

[144] J. R. Maze et al., "Properties of nitrogen-vacancy centers in diamond: The group theoretic approach," *New J. Phys.*, vol. 13, no. 2, Feb. 2011, Art. no. 025025, doi: 10.1088/1367-2630/13/2/025025.

[145] A. Albrecht, A. Retzker, F. Jelezko, and M. Plenio, "Coupling of nitrogen vacancy centres in nanodiamonds by means of phonons," *New J. Phys.*, vol. 15, no. 8, Aug. 2013, Art. no. 083014, doi: 10.1088/1367-2630/15/8/083014.

[146] E. Neu et al., "Single photon emission from silicon-vacancy colour centres in chemical vapour deposition nano-diamonds on iridium," *New J. Phys.*, vol. 13, Feb. 2011, Art. no. 025012, doi: 10.1088/1367-2630/13/2/025012.

[147] B. L. Green et al., "Neutral silicon-vacancy center in diamond: Spin polarization and lifetimes," *Phys. Rev. Lett.*, vol. 119, Aug. 2017, Art. no. 096402, doi: 10.1103/PhysRevLett.119.096402.

[148] D. D. Sukachev et al., "Silicon-vacancy spin qubit in diamond: A quantum memory exceeding 10 ms with single-shot state readout," *Phys. Rev. Lett.*, vol. 119, Nov. 2017, Art. no. 223602, doi: 10.1103/PhysRevLett.119.223602.

[149] G.-Q. Liu et al., "Single-shot readout of a nuclear spin weakly coupled to a nitrogen-vacancy center at room temperature," *Phys. Rev. Lett.*, vol. 118, Apr. 2017, Art. no. 150504, doi: 10.1103/PhysRevLett.118.150504.

[150] C. Bradley et al., "A ten-qubit solid-state spin register with quantum memory up to one minute," *Phys. Rev. X*, vol. 9, no. 3, Sep. 2019, Art. no. 031045, doi: 10.1103/PhysRevX.9.031045.

[151] H. P. Bartling et al., "Entanglement of spin-pair qubits with intrinsic dephasing times exceeding a minute," *Phys. Rev. X*, vol. 12, 2022, Art. no. 011048, doi: 10.1103/PhysRevX.12.011048.

[152] G. Zhang, Y. Cheng, J.-P. Chou, and A. Gali, "Material platforms for defect qubits and single-photon emitters," *Appl. Phys. Rev.*, vol. 7, Sep. 2020, Art. no. 031308, doi: 10.1063/5.0006075.

[153] T. T. Tran, K. Bray, M. J. Ford, M. Toth, and I. Aharonovich, "Quantum emission from hexagonal boron nitride monolayers," *Nature Nanotechnol.*, vol. 11, no. 1, pp. 37–41, Jan. 2016, doi: 10.1038/nnano.2015.242.

[154] L. J. Martínez et al., "Efficient single photon emission from a high-purity hexagonal boron nitride crystal," *Phys. Rev. B*, vol. 94, Sep. 2016, Art. no. 121405, doi: 10.1103/PhysRevB.94.121405.

[155] R. Bourrellier et al., "Bright UV single photon emission at point defects in h-BN," *Nano Lett.*, vol. 16, no. 7, pp. 4317–4321, Jul. 2016, doi: 10.1021/acs.nanolett.6b01368.

[156] P. Tonndorf et al., "Single-photon emission from localized excitons in an atomically thin semiconductor," *Optica*, vol. 2, no. 4, pp. 347–352, Apr. 2015, doi: 10.1364/OPTICA.2.000347.

[157] A. Srivastava, M. Sidler, A. V. Allain, D. S. Lembke, A. Kis, and A. Imamoğlu, "Optically active quantum dots in monolayer WSe_2," *Nature Nanotechnol.*, vol. 10, no. 6, pp. 491–496, Jun. 2015, doi: 10.1038/nnano.2015.60.

[158] M. Koperski et al., "Single photon emitters in exfoliated WSe_2 structures," *Nature Nanotechnol.*, vol. 10, no. 6, pp. 503–506, Jun. 2015, doi: 10.1038/nnano.2015.67.

[159] C. Chakraborty, L. Kinnischtzke, K. M. Goodfellow, R. Beams, and A. N. Vamivakas, "Voltage-controlled quantum light from an atomically thin semiconductor," *Nature Nanotechnol.*, vol. 10, no. 6, pp. 507–511, Jun. 2015, doi: 10.1038/nnano.2015.79.

[160] Y.-M. He et al., "Single quantum emitters in monolayer semiconductors," *Nature Nanotechnol.*, vol. 10, no. 6, pp. 497–502, Jun. 2015, doi: 10.1038/nnano.2015.75.

[161] S. I. Azzam, K. Parto, and G. Moody, "Prospects and challenges of quantum emitters in 2D materials," *Appl. Phys. Lett.*, vol. 118, no. 24, Jun. 2021, Art. no. 240502, doi: 10.1063/5.0054116.

[162] S. M. de Vasconcellos, D. Wigger, U. Wurstbauer, A. W. Holleitner, R. Bratschitsch, and T. Kuhn, "Single-photon emitters in layered van der Waals materials," *Phys. Status Solidi B*, vol. 259, no. 4, Jan. 2022, Art. no. 2100566, doi: 10.1002/pssb.202100566.

[163] Z. Peng, X. Chen, Y. Fan, D.J. Srolovitz, and D. Lei, "Strain engineering of 2D semiconductors and graphene: from strain fields to band-structure tuning and photonic applications," *Light Sci. Appl.*, vol. 9, no. 1, pp. 1–25, Nov. 2020, doi: 10.1038/s41377-020-00421-5.

[164] J. Klein et al., "Site-selectively generated photon emitters in monolayer MoS_2 via local helium ion irradiation," *Nature Commun.*, vol. 10, no. 2755, pp. 1–8, Jun. 2019, doi: 10.1038/s41467-019-10632-z.

[165] O. Iff et al., "Strain-tunable single photon sources in WS monolayers," *Nano Lett.*, vol. 19, no. 10, pp. 6931–6936, Sep. 2019, doi: 10.1021/acs.nanolett.9b02221.

[166] H. Kim, J. S. Moon, G. Noh, J. Lee, and J.-H. Kim, "Position and frequency control of strain-induced quantum emitters in WSe_2 monolayers," *Nano Lett.*, vol. 19, no. 10, pp. 7534–7539, Sep. 2019, doi: 10.1021/acs.nanolett.9b03421.

[167] T. T. Tran et al., "Robust multicolor single photon emission from point defects in hexagonal boron nitride," *ACS Nano*, vol. 10, no. 8, pp. 7331–7338, Jul. 2016, doi: 10.1021/acsnano.6b03602.

[168] G. Grosso et al., "Tunable and high-purity room temperature single-photon emission from atomic defects in hexagonal boron nitride," *Nature Commun.*, vol. 8, no. 1, pp. 1–8, Sep. 2017, doi: 10.1038/s41467-017-00810-2.

[169] T. T. Tran et al., "Quantum emission from defects in single-crystalline hexagonal boron nitride," *Phys. Rev. Appl.*, vol. 5, Mar. 2016, Art. no. 034005, doi: 10.1103/PhysRevApplied.5.034005.

[170] J. A. Preuß, E. Rudi, J. Kern, R. Schmidt, R. Bratschitsch, and S. M. de Vasconcellos, "Assembly of large hBN nanocrystal arrays for quantum light emission," *2D Mater.*, vol. 8, no. 3, Mar. 2021, Art. no. 035005, doi: 10.1088/2053-1583/abeca2.

[171] A. Hernández-Mínguez, J. Lähnemann, S. Nakhaie, J. M. J. Lopes, and P. V. Santos, "Luminescent defects in a few-layer h-BN film grown by molecular beam epitaxy," *Phys. Rev. Appl.*, vol. 10, Oct. 2018, Art. no. 044031, doi: 10.1103/PhysRevApplied.10.044031.

[172] B. Lounis and M. Orrit, "Single-photon sources," *Rep. Prog. Phys.*, vol. 68, no. 5, pp. 1129–1179, Apr. 2005, doi: 10.1088/0034-4885/68/5/R04.

[173] M. Koperski, K. Nogajewski, and M. Potemski, "Single photon emitters in boron nitride: More than a supplementary material," *Opt. Commun.*, vol. 411, pp. 158–165, Mar. 2018, doi: 10.1016/j.optcom.2017.10.083.

[174] G. Noh et al., "Stark tuning of single-photon emitters in hexagonal boron nitride," *Nano Lett.*, vol. 18, no. 8, pp. 4710–4715, Aug. 2018, doi: 10.1021/acs.nanolett.8b01030.

[175] N. Mendelson, M. Doherty, M. Toth, I. Aharonovich, and T. T. Tran, "Strain-induced modification of the optical characteristics of quantum emitters in hexagonal boron nitride," *Adv. Mater.*, vol. 32, no. 21, Apr. 2020, Art. no. 1908316, doi: 10.1002/adma.201908316.

[176] D. Scolfaro et al., "Acoustically driven stark effect in transition metal dichalcogenide monolayers," *ACS Nano*, vol. 15, no. 9, pp. 15371–15380, Sep. 2021, doi: 10.1021/acsnano.1c06854.